# Subsurface Lithologic Controls on Off-Fault Deformation and Multi-Fault Slip During the 2016 Mw 6.5 Norcia Earthquake Revealed by Satellite Geodesy

Mathilde Marchandon, James Hollingsworth, Louise Maubant, Anne Socquet, Erwan Pathier, Mathilde Radiguet, and Alice-Agnes Gabriel

# Subsurface Lithologic Controls on Off-Fault Deformation and Multi-Fault Slip During the 2016 Mw 6.5 Norcia Earthquake Revealed by Satellite Geodesy

**Mathilde Marchandon[1], James Hollingsworth[2], Louise Maubant[3], Anne Socquet[2], Erwan Pathier[2], Mathilde Radiguet[2], and Alice-Agnes Gabriel[4,1]**

[1]Department of Earth and Environmental Sciences, Ludwig-Maximillians-Universität München, Munich, Germany
[2]Univ. Grenoble Alpes, Univ. Savoie Mont Blanc, CNRS, IRD, Univ. Gustave Eiffel, ISTerre, Grenoble, France
[3]Earthquake Research Institute,The University of Tokyo, Tokyo, Japan
[4]Scripps Institution of Oceanography, UC San Diego, La Jolla, USA

**Key Points:**

- Analysis of a new high-resolution optical displacement field reveals 46% of off-fault deformation (OFD)
- Near-surface lithology exerts a first-order control on OFD, while effect of segments orientation with respect to the stress field is limited
- A new multi-fault slip model reveals 72% of Shallow Slip Deficit (SSD) on average and no correlation between the amount of SSD and OFD

---

Corresponding author: Mathilde Marchandon, `M.Marchandon@lmu.de`

## Abstract

Understanding the mechanisms controlling deformation localization is crucial for our understanding of fault mechanics and improving seismic hazard assessment, but has not been extensively studied for normal-faulting earthquakes. Here, we present a thorough analysis of the 2016 Mw 6.5 Norcia, Italy, earthquake using high-resolution satellite geodesy. We investigate the degree of deformation localization, evaluate its controlling factors and the link with the distribution of slip with depth. Using the optical image correlation technique with an innovative method for noise correction, we measure the near-field 3D displacements associated with the Norcia event. Based on these measurements, we quantify the amount of off-fault deformation (OFD) and evaluate how it varies with external factors. We find 46% (25 cm) of OFD on average and a strong correlation with local topographic slope and near-surface lithology, with increased distributed deformation where ruptures traverse unconsolidated sediments and areas of gentler slopes. In contrast, the correlation between OFD and the fault segment orientation relative to the regional stress field is weak. We develop a comprehensive slip model accounting for complex multi-segmented fault geometry, topography, and 3D elastic structure through a joint inversion of optical, InSAR, and GPS data. The inversion reveals a highly heterogeneous slip distribution characterized by large slip (up to 3.5 m) at depth, and several shallow slip patches. We find a pronounced average shallow slip deficit (SSD) of 72%, with no along-strike correlation between SSD and OFD. This suggests that the OFD primarily reflects surficial inelastic processes occurring within the shallow soil.

## Plain Language Summary

In this study, we use high-resolution satellite images to measure the 3D displacements of the ground produced by the 2016 Mw 6.5 Norcia earthquake, Italy. Our main goal is to understand whether the deformation is focused directly on the fault or spread out in the surrounding areas, and what factors influenced this pattern. We found that nearly half (about 46%) of the deformation occurred off the main fault. This off-fault deformation is more common in areas with softer surface materials and gentler slopes, while the orientation of the fault in relation to regional stress does not appear to have a significant impact. Combining satellite and GPS data, we create a detailed model of how the fault slipped at depth during the earthquake. We find that most of the slip happened at depth (up to 3.5 m at 5 km depth), with less movement near the surface, a pattern known as a shallow slip deficit (about 72% less slip at shallow depths). The amount of surface off-fault deformation does not match up with the missing shallow slip. This suggests that the off-fault deformation we measure may reflect inelastic processes occurring at very shallow depths (i.e. within the soil).

## 1 Introduction

It has long been known that coseismic deformation at shallow depths is partitioned between frictional slip on well-defined surfaces and distributed deformation in the volume around the fault (Nelson & Jones, 1987; Rockwell et al., 2002; Shelef & Oskin, 2010). Understanding what controls the degree of localization of deformation and how surface deformation relates to fault slip at depth is crucial not only for our understanding of fault mechanics but also to refine seismic hazard assessment. Indeed, if the distributed component of surface deformation is not taken into account when geological fault slip rates are evaluated, seismic hazard estimated using probabilistic approaches incorporating geological fault slip rates could be systematically underestimated (Dolan & Haravitch, 2014). Moreover, coseismic off-fault deformation impacts the intensity of ground shaking near the fault during an earthquake (Andrews, 2005; Roten et al., 2014, 2018), as well as rupture speed (sub- vs supershear) and style (pulse vs. crack) (Gabriel et al., 2013).

In recent years, near-fault displacement maps of surface-rupturing strike-slip earthquakes obtained from optical correlation have been extensively used to estimate the magnitude of deformation occurring both on (localized slip) and off (off-fault deformation, OFD) the main fault, to evaluate which parameters control the degree of localization of the deformation, and how off-fault deformation relates to the on-fault slip distribution with depth (e.g. Milliner et al., 2015; Zinke et al., 2014; Hollingsworth et al., 2017; Antoine et al., 2021; Scott et al., 2018a; Kuo et al., 2019; Hayek et al., 2024; Antoine et al., 2024). However, to date, no similar analysis has focused specifically on normal-faulting earthquakes.

Previous studies show that the amount of OFD vary both along fault ruptures and from one earthquake to another. Several parameters are thought to impact the degree of localization of deformation, such as the fault maturity (the higher is the maturity level, the more localized is the deformation, Dolan & Haravitch, 2014; Socquet et al., 2019; Li, Li, Shan, & Zhang, 2023; Milliner et al., 2025), fault geometrical complexities (with larger OFD found at fault complexities, Milliner et al., 2015; Antoine et al., 2022), the nature of the subsurface materials (Milliner et al., 2015), the orientation of the fault with respect to the stress field (optimally oriented segments would localize better the deformation, Liu-Zeng et al., 2024), and the earthquake magnitude (larger earthquakes would produce a lower amount of OFD). However, the underlying mechanisms responsible for the off-fault deformation remain unclear. Although OFD estimated from optical correlation data is often assumed to originate from inelastic processes occurring in the shallow crust (Scott et al., 2018a; Antoine et al., 2021), both inelastic and elastic processes can produce similar deformation pattern at the surface (Nevitt et al., 2020) and the respective contribution of each process is difficult to untangle (Hayek et al., 2024). Furthermore, different techniques exist to measure off-fault deformation from optical data, that generally lead to different amounts (e.g. 45% vs. 28% of OFD estimated for the Balochistan earthquake in Zinke et al. (2019) and Gold et al. (2015), respectively), potentially due to the fact that each technique is sensitive to different processes. OFD estimates can also be biased by the optical correlation technique itself. Indeed optical correlation techniques assume that all pixels undergo a homogeneous translation within a given correlation window, which biases the measure of the displacements near the fault when the correlation window crosses the fault (Montagnon et al., 2024). This can in turn lead to an overestimation of the OFD extent (Ajorlou et al., 2021). The interplay between OFD and the distribution of localized fault slip with depth, particularly with the shallow slip deficit (SSD, Fialko, 2004) is unclear as well, one reason being the difficulty to obtain a robust estimation of the one-fault slip. Indeed, a robust estimation of the distribution of the slip with depth is hindered by the ill-posed nature of the inverse problem, the simplified representation of the medium, the data quality and coverage, and the inaccurate representation of the fault geometry (X. Xu et al., 2016; Marchandon et al., 2021; Wang et al., 2024).

Fully understanding how the coseismic deformation is accommodated within active fault zones requires to investigate surface rupturing earthquakes in various tectonic context using both state-of-the-art imaging method to retrieve the deformation pattern in the near field, but also using inversion methods that account for medium complexities. In this study, we propose a thorough analysis of the 2016 Mw 6.3 Norcia normal-faulting earthquake, Central Apennines, Italy. We first measure the near-field 3D displacements of the Norcia event from the correlation of high-resolution Pleiades and Worldview optical images. We present an original method to correct the 3D displacement field from aliasing due to strong off-nadir acquisition of the satellite images. Based on our near-fault measurements, we estimate the amount of OFD and evaluate how it varies with external parameters (topographic slope, nature of subsurface materials). Then, we extend our analysis to the slip at depth from a joint inversion of optical, InSAR, and GPS data. We use an inversion method that takes into account the medium complexities (non-planar multi-segmented fault geometry, topography, and 3D medium properties) in order to infer an unbiased slip distribution. We then discuss the factors controlling off-fault deformation for the Norcia earthquake, the link between off-fault deformation and shallow slip deficit and potential avenues to further improve our understanding of the mechanical behavior of the shallow crust.

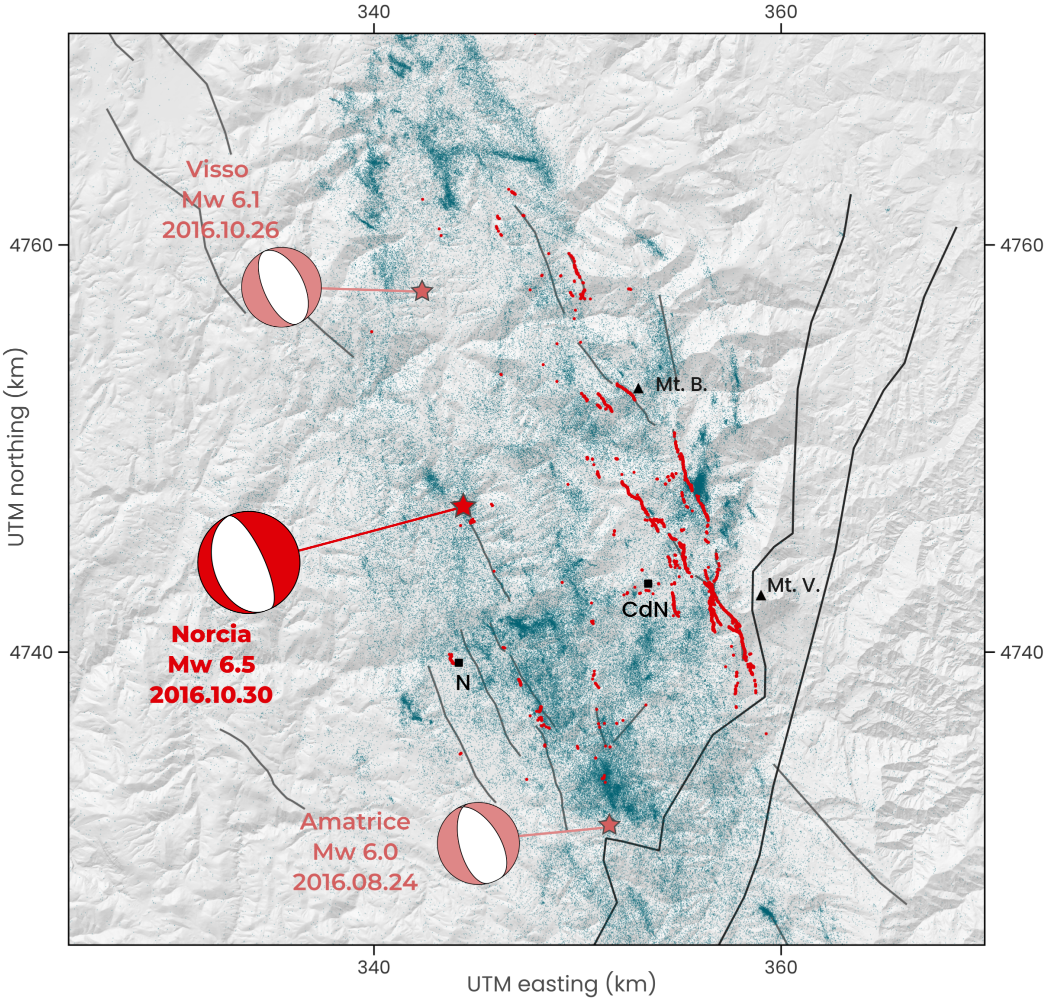

**Figure 1.** Tectonic setting of the 2016 central Apennines earthquake sequence. Thin gray lines show the main active normal faults while the tick gray lines show the northwestern dipping Sibillini thrusts. The red lines show the surface rupture traces produced by the Norcia event mapped in the field (Villani et al., 2018). The stars locate the epicenters of the Amatrice, Visso and Norcia earthquakes. The focal mechanisms are from USGS. The dark green dots represent the aftershocks of the sequence between 24.08.2016 to 31.08.2017 (Waldhauser et al., 2021). N and CdN locates the towns of Norcia and Castelluccio di Norcia, while Mt B and Mt V locate the Monte Bove South and the Monte Vettore, respectively.

## 2 The 2016 Mw 6.5 Norcia Earthquake

The 2016 Central Apennines earthquake sequence took place in Central Italy and consisted of three large normal-fault earthquakes that broke the WSW-dipping Mt. Vettore–Mt. Bove fault system (VBFS) (Chiaraluce, Stefano, et al., 2017, Figure 1). The sequence began with the Mw 6.2 Amatrice earthquake, which ruptured the south part of the VBFS. Two month later, on the 26th of October, the Mw 6.1 Visso earthquake broke the northern part of the VBFS. The Mw 6.5 Norcia earthquake occurred two days after the Visso earthquake, rupturing the central section of the VBFS and reactivating a part of the fault previously ruptured by the Amatrice earthquake. The 2016 sequence was followed, on the 18th of January 2017, by a sequence of four Mw 5.1-5.5 earthquakes that ruptured the Campotosto fault system, located south of the Monte Vettore fault system and north of the Paganica fault, which hosted the 2009 Mw 6.3 l'Aquila earthquake (Falcucci et al., 2018). Although there are clear geomorphic evidences of paleoseismic activity on the VBFS (i.e. Cello et al., 1997; Galadini & Galli, 2000), no historical or instrumental records document a large earthquake on this fault system prior to the 2016 sequence.

The sequence produced a complex network of surface ruptures over a length of about 30 km, among which ∼20 km result from the Norcia earthquake alone (Brozzetti et al., 2019; Civico et al., 2018; Villani et al., 2018). The surface rupture network of the Norcia event is composed of several segments that follow the geological trace of the VBFS, as well as several synthetic and antithetic secondary segments located on the VBFS hanging wall (Villani et al., 2018; Brozzetti et al., 2019, Figure 1). Field measurements reveal average surface offsets of ∼30 cm, reaching up to 2.2 m locally on the western flank of the Monte Vetorre (Villani et al., 2018; Brozzetti et al., 2019).

Previous slip models for the Norcia earthquake obtained from seismic and/or geodetic data show that most of the slip was concentrated in one main asperity located between 3 and 7 km depths with a maximum slip amplitude in the range 2.5-4 m (Chiaraluce, Di Stefano, et al., 2017; Cheloni et al., 2017; Pizzi et al., 2017; G. Xu et al., 2017; Scognamiglio et al., 2018; Walters et al., 2018; Delorme et al., 2020). Additionally, some studies suggest that slip is needed either on an antithetic NE-dipping fault or on the shallow-dipping Sibillini thrust to fully explain InSAR data (Cheloni et al., 2017; Scognamiglio et al., 2018). The mechanical viability of the two-fault slip model proposed by Scognamiglio et al. (2018), involving the VBFS and the Sibillini thrust, was validated through dynamic rupture simulations (Tinti et al., 2021). Most previous studies, however, used a simplified fault geometry consisting of one planar segment to model the VBFS, limiting the ability to meaningfully compare subsurface slip and slip at depth. Notable exceptions are Delorme et al. (2020) and Walters et al. (2018) whose use multiple planar segments to model the main fault along with secondary segments in the hanging-wall.

To the best of our knowledge, only three studies have geodetically analyzed the near-fault deformation pattern of the Norcia earthquake. Delorme et al. (2020) used optical correlation to measure the near-fault displacement field of the entire rupture and found that the fault offsets measured from the optical correlation displacement maps tend to be consistent or larger than the field measurements. Wedmore et al. (2019) used pre- and post-earthquake terrestrial laser scanning point clouds to measure centimeter-scale surface displacements along a 150 m long section of the Norcia rupture. They estimated that 50% of the horizontal deformation was distributed within 8 m of the fault while the vertical component exhibits a smaller amount of OFD (16%) within a narrower zone (4 m). Carboni et al. (2022) used ALOS-2 interferograms to identify a large number of surface ruptures and found them to be in agreement with those mapped in the field.

# 3 Method

## 3.1 Analysis of Near-Fault Displacements

### *3.1.1 Optical Data Processing*

To document the surface displacement field produced by the 24th October Mw 6.5 Norcia earthquake, we correlate pre-earthquake tri-stereo Pleiades satellite images (acquired the 29th of October 2016, Table S1) with post-earthquake stereo WorldView-2 images (acquired the 1st of November 2016). The very short temporal baseline of 3 days is important for minimizing correlation bias associated with differential illumination conditions, which can be more extreme in winter months when the lower sun elevations give rise to stronger shadows. Furthermore, snowfall in the epicentral region soon after the mainshock, prevented further acquisition of imagery in the early post-seismic period.

We follow the 3D correlation methodology of Zinke et al. (2019). We first orthorectify a reference image (the left image of the pre-earthquake stereo pair) using a medium resolution DEM (AW3D30, 30m resolution). We then coregister all other images (pre-right, post-left, and post-right) relative to the reference, and orthorectify them all using the same medium resolution DEM. We then correlate each orthoimage relative to the reference. Using the satellite positions and the various correlation maps, we can solve the 3D ground position at each pixel on the correlation grid using a basic ray tracing approach (Avouac & Leprince, 2015; Marchandon et al., 2022).

Because the post-earthquake WorldView-2 images were tasked rapidly for disaster response efforts, the stereo acquisition parameters were not optimal for stereo-matching and DEM generation. The incidence angles were strongly off-nadir (left and right image view angles: -16.5° and -11.3° (along-track) and 37.9° and 38.7° (across-track). Consequently, the ground sampling of each WorldView image is strongly dependent on the topography, e.g. when the topographic slope is not perpendicular to the satellite look angle, the ground sampling density will be less than the slope-perpendicular case. Therefore, due to the strong off-track viewing geometry, the ground sampling on east versus west-facing slopes is starkly different. During the orthorectification stage, which is required to remove the large stereoscopic signals within the images prior to ground displacement correlation, this irregular sampling produces strong aliasing signals in the final orthorectified images. This problem can be somewhat mitigated by orthorectifying at a lower resolution, although we then lose the ability to resolve the small ground displacements. To overcome this problem, we make use of a second stereo acquisition of Pleiades satellite images (from 13th September 2017). By correlating the post-WorldView with the post-Pleiades images, we capture this aliasing signal, along with any minor post-seismic deformation (which is generally below the detection threshold of image correlation, unlike the much larger co-seismic signal). We use Independent Component Analysis (FastICA) to isolate the spatial map of the aliasing component. We then solve for a coefficient which, when multiplied with the aliasing component and subtracted from the original 3D co-seismic displacement components (high-pass filtered, to minimize the coseismic signal), minimizes the global standard deviation. This adjusted aliasing map can then be removed from the relevant pre-Pleiades-post-WorldView displacement component. This approach proves highly effective at reducing the amplitude of the aliasing signal, which would otherwise overwhelm the earthquake displacement (Figure S1). Because the aliasing signal is isolated from postseismic images using ICA, we are confident that we do not introduce any postseismic signal to our coseismic correction. Furthermore, careful analysis of the aliasing component does not reveal any steps along the fault rupture location. Finally, we denoise outliers from the displacement map using a local neighborhood statistical method (Zinke et al., 2019), as well as removing long-wavelength jitter signals using simple destriping (Ayoub et al., 2017).

We find that the 3D displacement map produced from pre-Pleiades and post-WorldView-2 imagery is superior to that from pre-Pleiades and post-Pleiades (which includes 10 months of postseismic deformation). This is likely due to the similar illumination conditions between the pre-Pleiades and post-WorldView images, which yields cleaner displacements less corrupted by illumination bias. Also, the short temporal baseline allows us to better isolate the coseismic response of the Norcia mainshock, which is of prime interest in this study.

#### *3.1.2 Optical Offset and Off-Fault Deformation Measurement*

We mapped the various surface rupture traces of the Norcia earthquake by identifying sharp discontinuities in the EW, NS, and vertical displacement maps. To measure the amplitude and evaluate the variability of the surface fault slip along the various mapped segments, we measured the fault offsets using 2 km long stacked profiles spaced every 80 m. The choice of the stack width is a compromise between the signal over noise ratio and the along-strike offset variability we want to resolve. The larger is the stack width, the higher is the signal over noise ratio, and the smoother is the obtained along strike offset variations. Here, for most segments, the offsets we want to measure are of the same order of magnitude than the noise in the data. We thus choose a stack width of 408 m (51 pix). Consequently, each stacked profile is not independent from the neighboring one and independent stacked profiles are obtained every 5 measurements (= stack width/step). The offsets across the fault are then measured from the relative difference at the fault between linear regressions fitted on each side of the fault (e.g. Milliner et al., 2015). Note that we made sure the along-strike width over which the profiles was stacked does not encompass a significant fault strike variation that could bias the offset measurements. In total, 222 offsets were measured.

The common practice to estimate the uncertainty of the measured offset is to use the misfit of the linear regression (e.g. Marchandon et al., 2018). However, the error obtained from this method does not reflect the uncertainty due to the subjective choices made when one measures offset from displacement profiles. Therefore, here we append a confidence level value to each offset depending on the degree of confidence we have about each offset measurement. A value of 1 means that the fault offset is easily identified and the offset value does not depend on the portions of the fault use to compute the linear regression. A value of 2 means that the offset is quite clear and well discernible from the noise but, depending on the points used to compute the regression, the value can slightly change. Finally, a value of 3 means the offset is hardly discernible from the noise and/or does not make a clear scarp on the fault. Consequently, the value obtained depends significantly on the portions of the fault chosen to compute the linear regression. Figure S3 shows examples of profile representative of the three different categories and Figure S4 shows the confidence level value for each measured offset. Most offsets have a confidence value of 1 or 2 while only 25 (over 222) offsets have a confidence value of 3. The latter are plotted with a low level of opacity in Figure 3. We note that most offsets having a low confidence value are low amplitude offsets ($< 0.25$ m).

To estimate the amount of off-fault deformation (OFD), we compare the optical offsets with the offsets measured in the field. This is a widely used method to estimate OFD (e.g. Milliner et al., 2015; Zinke et al., 2014; Ajorlou et al., 2021; Li, Li, Shan, & Zhang, 2023). The rational is that the offsets measured from optical correlation encompass the total shear across the fault zone while in the field, only the localized component of the slip is measured. We use the field offsets from the database of Villani et al. (2018), consisting of 7323 observations. Among these 7323 field observations, we select the ones for which the throw (i.e. vertical displacement across the fault) was given and compare them with the optical offset measured from our vertical displacement map. Offsets measured in the field are isolated measurements only representative of the discrete locations where the measurements were made. On the contrary, offsets measured from optical correlation map are representative of a larger spatial scale, the extent of which is controlled by the various parameters that come into play during the correlation and offset measurements processes (e.g. image resolution, correlation windows size, step size, and stack width used when measuring the profiles). Comparing these two types of data is thus not straightforward. In order to make a meaningful comparison of the field and optical data sets, for each stack profile we compute the average of the field offsets located within the range of the stack box. This method is appropriate because field measurements for the Norcia earthquake are dense and sufficiently evenly distributed along each fault segment. Doing this, we aim at suppressing the along-strike difference of spatial scale between the two data sets such that any difference between the optical and field offsets reflects rupture-related processes.

## 3.2 Slip Distribution at Depth

### *3.2.1 Data*

To retrieve the fault slip distribution for the Norcia earthquake, we perform a joint inversion of optical, InSAR, and GPS data. The GPS dataset has been downloaded from the Rete Integrata Nazionale GPS (RING) website (http://ring.gm.ingv.it) and is composed of 115 three-component displacement points (Figure 9). The InSAR dataset is composed of two ascendant and one descendant ALOS-2 interferograms (Table S2). We compute the interferograms using the GMTSAR processing chain (Sandwell et al., 2011). The topographic phase contribution is removed from the interferograms using the Shuttle Radar Topography Mission 3 arc-sec (∼90 m resolution) DEM (SRTM; Farr et al., 2007). The interferograms are filtered using a coherence-dependent filter and unwrapped using a branch-cut algorithm (Goldstein et al., 1988). Two of the three interferograms (T92D and T197A, Table S2) encompass also the Visso earthquake, that occurred 2 days before the Norcia earthquake and that broke 15 km of the northern continuation of the Monte-Bove Monte-Vettore fault system (Figure 1). Therefore, as a preliminary step, we estimate and remove the contribution of the Visso earthquake from the concerned interferograms by performing a joint inversion for both the Visso and Norcia slip distribution. The details of the methodology used to perform this preliminary step is described in the Supplementary Text S1. As a result, the interferograms used in the following are cleared from the contribution of the Visso earthquake. Finally, the optical dataset is composed of the EW, NS, and vertical displacement fields. Both the InSAR and optical data sets have been subsampled using a scheme that depends on the distance to the fault, allowing to keep a dense data coverage near the fault while reducing the redundant information provided by data point located in the far-field. For the InSAR dataset, we kept one point every 2 km within 17 km from the fault, one point every 5 km for distances between 17 and 21 km from the fault, and one point every 10 km for distances farther than 21 km. For the optical data set, we kept one point every 200 m within 1.5 km from the fault, one point every 500 m for distances between 1.5 km and 3 km, and one point every kilometer for distance larger than 3 km. We choose this subsampling method rather than the more classically used quadtree algorithm to avoid smoothing the fault step in the optical displacement field, which could in turn bias the estimation of the subsurface fault slip.

### *3.2.2 Inversion Method*

The Green's functions, that relate the surface displacements to the fault slip, are computed using the Finite Element Model Pylith (Aagaard et al., 2013) and take into account the topography and the 3D variations in elastic properties of the Norcia region. The mesh of the finite element model is built using the Trelis software. The dimension of the mesh is 500 km x 500 km x 500 km along the east, north, and vertical direction. We model the topography using the SRTM DEM dowsampled at 1 km and we derive the elastic properties from the 3D velocity model of Chiarabba et al. (2018). The fault model is composed of three non-planar fault segments that follow the surface rupture trace mapped on the optical correlation maps (Figure S2c). The first segment is 43 km long and models the main fault, the second segment is 5 km long and models the synthetic secondary segments near the Monte-Vettore, and the third segment is 5 km long and models a secondary antithetic segment (Figure S2c). At the surface, the segments match the surface rupture trace, whereas at depth the geometrical complexities are progressively smoothed (see Figure S7 for a 3D representation of the fault segments). Near Monte Vettore, the distance between the main fault and the secondary synthetic segment is very small (down to ∼70 m), implying that this part has to be meshed using considerably smaller cells than elsewhere. This renders the production of a high quality mesh more challenging. To overcome this problem, we build three different meshes, one for each fault segment, all having the same size and similar discretization parameters. To balance computational efficiency with accuracy, we use a heterogeneous mesh. The cell size is 700 m on average on the fault at shallow depths, increases to 1.5 km at the bottom of the fault, and gradually increases to 20 km toward the model boundaries. To evaluate the accuracy of our finite element model, we compute the surface displacements at the surface caused by one meter of dip-slip on the Monte Vettore fault, using both the analytical Okada solution and our FEM, the latter assuming a homogeneous elastic medium and a flat (no topography) surface. The differences between the Okada and FEM solutions are minimal, indicating that our FEM achieves sufficient accuracy.

To evaluate the resolving power of each dataset, we compute the data sensitivity (Loveless & Meade, 2011). This parameter quantifies the sensitivity of the surface deformation to the slip on each subfault and helps identify which parts of the model are well constrained. The sensitivity is defined as the sum of the surface displacements at all data points induced by a unit slip on the considered patch divided by the number of data:

$$S_k = \frac{\sum_{i=1}^{N} u_{s,i} + \sum_{i=1}^{N} u_{d,i}}{N}. \tag{1}$$

where $S_k$ is the sensitivity of the $k^{th}$ subfault, $u_{s,i}$ and $u_{d,i}$ are the surface displacement for the data point $i$ due to 1 m of strike-slip and dip-slip, respectively, on subfault $k$, and $N$ the number of surface data. The sensitivity distributions for the main and secondary faults, as well as for each dataset, are shown in Figures S8 and S9. For the optical dataset, sensitivity is highest within the first two kilometers depth, reaching up to 5 m. At greater depths, it decreases, averaging around 1.5 m. Beyond approximately 6.5 km depth, the resolving power of the optical data becomes very low, with sensitivities dropping below 0.5 m (Figure S8a). In contrast, the sensitivity of the InSAR dataset is more uniform, averaging around 1 m (Figure S8b). Unlike the optical data, InSAR sensitivity is low in the upper two kilometers (<0.5 m), highlighting the complementarity between the two datasets. For the GPS dataset, sensitivity is very low (<0.1 meters), primarily due to the sparse distribution of GPS stations in the near-field region (Figure S8c). The antithetic and synthetic faults are mainly constrained by the optical dataset, with sensitivity values reaching up to 2.2 m and 1.1 m, respectively (Figure S9).

The slip on the fault is retrieved using a constrained least square inversion (Coleman & Li, 1996). The normal slip is constrained between 0 and 15 m, the strike-slip is constrained between -5 and 5 m and a smoothing operator is implemented to avoid unrealistic slip variations between neighboring patches (Jónsson et al., 2002). Preliminary inversion tests showed that a classical Laplacian smoothing operator strongly decreased the fit to the near-fault optical data without smoothing significantly the slip distribution at depth. To overcome this issue we implement a smoothing operator that varies with depth such as the slip distribution is less strongly smoothed at the surface than at depth. We also solve for a plane on the three interferograms and the EW, NS, Z optical displacement fields in order to correct for any residuals orbital or registration errors (e.g. Sudhaus & Jonsson, 2011) that can affect the consistency between the different datasets. Finally, the data are weighted such that each data set is equally well fitted. The data weighting takes into account the number of data points within each data set such that data sets with a lower number of points are not under-weighted in the inversion. We thus resolve the following system of equations:

$$\begin{bmatrix} \mathbf{d}' \\ 0 \end{bmatrix} = \begin{bmatrix} \mathbf{G}' \\ \lambda \mathbf{D} \end{bmatrix} \mathbf{m} \tag{2}$$

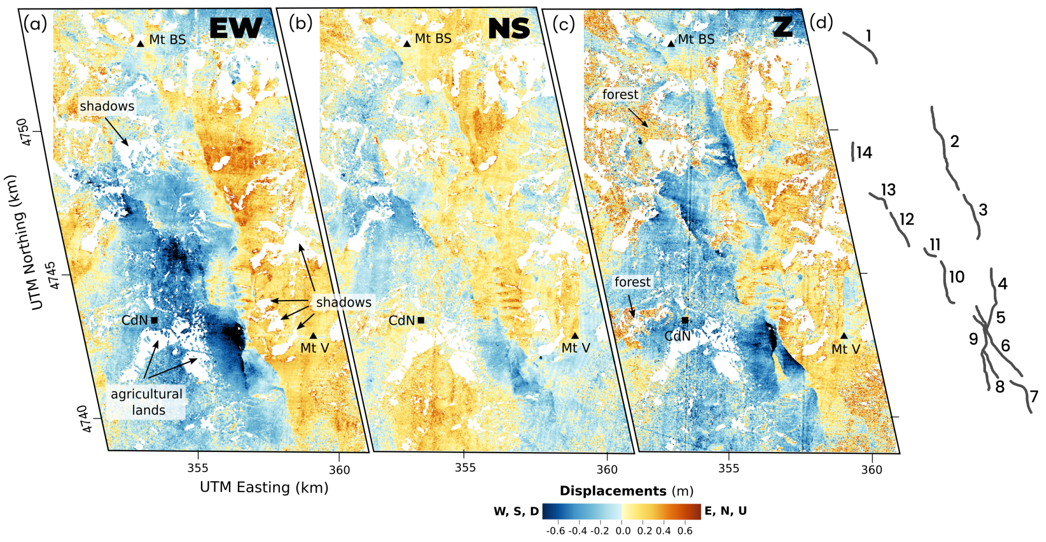

**Figure 2.** 3D displacement field of the Norcia earthquake obtained from the correlation of high-resolution optical Pleaides and Worldview-2 imagery. (a) EW displacements (positive eastward) (b) NS displacements (positive northward) (c) Vertical displacements (positive upward). (d) Surface rupture map with segment numbering. CdN locates the town of Castelluccio di Norcia, while Mt BS and Mt V locate the Monte Bove South and the Monte Vettore, respectively.

with $\mathbf{d'} = \mathbf{wd}$, $\mathbf{G'} = \mathbf{wG}$, and where $\mathbf{d}$ is the data vector, $\mathbf{G}$ is the Green's functions matrix relating the surface data to the slip on each subfault, $\mathbf{w}$ is the vector describing the weight of each data point, $\mathbf{m}$ is the vector of parameters we are solving for (two components of slip on each sub-fault), $\mathbf{D}$ the second-order finite difference operator, and $\lambda$ the smoothing factor. We set $\lambda$ according to an L-curve criterion (Figure S10).

The best dip angle for each segment is determined in a preliminary step. Assuming a semi-infinite homogeneous elastic half-space (Okada, 1992), we run several inversions varying the dip angle value of each segment. We test dip angle values ranging from 34°W to 46°W for the main segment, 25°W to 50°W for the synthetic secondary segment and, 30°E to 80°E for the antithetic secondary segment. The best fitting dip angle is 40°W, 30°W, 40°E for the main, synthetic, and antithetic segments respectively (Figures S11-S13). Additionally, the first kilometer of the main fault has a steeper dip angle (∼70°) to match the values measured in the field (Villani et al., 2018).

# 4 Results

## 4.1 3D Displacement Field, Fault Offsets, & Off-Fault Deformation

The EW, NS, and vertical optical displacement fields of the Norcia earthquake are visible in Figure 2 and show a complex network of discontinuous N130°-N160° striking surface ruptures distributed over a width of ∼4 km. We identified 14 segments, 7 segments, striking approximately N160°, are located along the main Monte Vettore-Monte Bove fault (segments 1-7; Figures 2 & 3a) and 7 are located within its hanging-wall (segments 8-14, Figures 2 & 3a). The comparison of the horizontal and vertical displacement values on both sides of each segment allow identifying four antithetic (8, 11-13) and three synthetic (9,10,14) segments to the main fault. Generally, both the location and the dipping direction of the various mapped segments are consistent with field observations (Figure S2a,b).

Overall the displacement pattern in the EW and vertical maps is dominated by the deformation associated with the Mt Vettore-Mt Bove fault: its foot-wall globally moves westward and downward (blue area in Figure 2a and 2c) while its hanging-wall moves eastward and upward (eastern reddish area in Figure 2a and 2c). Due to the earthquake normal mechanism and the NW-SE orientation of the involved faults, the displacement amplitude in the NS direction is significantly smaller than in the EW and vertical components, and the surface ruptures are more difficult to detect. Nonetheless, the rupture traces of the segments 1-2 and 12-13 can still be clearly identified on the NS displacement field. Moreover, the strong signal associated with the segment 2 on the Mt Vettore-Mt Bove fault, which is nearly NS oriented, suggests that the slip on this part of the fault has a significant strike-slip component.

The optical and averaged field offsets along with the difference between the two datasets are plotted in Figure 3. The offsets measured on the segment belonging to the main fault and those measured on the subsidiary segments located within the main fault hanging-wall are plotted in different subplots for visibility (Figures 3b and 3c, respectively). When considering all segments, the mean optical offset is 47 cm whereas the mean value of the averaged field offsets is 36 cm. The mean and maximum offsets for each dataset and segment are provided in Table S3. Maximum offset values are found for both datasets on segment 6, in the western flank of the Mont Vettore and reach 111 cm and 147 cm for the optical and averaged field offsets, respectively (260 cm for the raw field offset). Regarding the comparison between the two data sets, three distinct cases are identified. In the first case, optical and field offsets are consistent. A representative example is segment 1, where the field and averaged field offsets closely match, and the raw field offsets are scattered, both above and below the optical offset values. Similar consistency is observed in segment 4 and at the northern tip of segment 7 (over a length of ∼500 m). In the second and most common case, the optical offsets are higher than the averaged field offsets and the raw field offsets lie almost systematically under the curve formed by the optical offsets. This situation occurs in segments 2, 3, 8, 9, 12, 13, at the southern tip of segment 7 and at the northern tip of segments 10 and 11. The mean difference between optical and averaged field offsets is 24.5 cm, indicating 46 % of OFD. Finally, the last situation is when the field offsets exceed the optical offsets. This case is encountered only in segment 6 and to a lesser extent in segment 10. In segment 6, the average field offset is 88 cm, while it is 64 cm for the optical offsets. The raw field offsets in this segment reach up to 2.60 m and are predominantly located above the optical offset curve.

In order to identify potential factors controlling the amount of OFD, we plot the difference between optical and field offsets against the topographic slope. For each stacked profile, we compute the mean topographic slope along the fault trace within the range of the stack profile box using a 10 m resolution DEM. The results, plotted on Figure 4a, show a clear linear trend: the lower the topographic slope, the greater the discrepancy between optical and field offsets. This trend appears more clearly when only high-confidence offsets are considered (type 1)(Figure 4b). We note that the averaged field offsets exceed the optical offsets exclusively in steep terrain (slope $> 30°$-$35°$).

We also compare the differences between optical and field offsets with the surface lithology. We use the information in the Villani et al. (2018) database to classify the fault offsets into three categories. We assign the fault offsets into the "bedrock/bedrock" category (B/B) when the rupture goes mainly through bedrock, to the "unconsolidated materials and soils" category (S/S) when the rupture goes mainly through unconsolidated material and soils and to the "bedrock/unconsolidated materials and soils" category (B/S) for the parts of the rupture where unconsolidated material and soils juxtaposes against bedrock. A map of the classification is shown in Figure S14 while the average difference between optical and field offsets as a function of the contact type is shown in Figure 5. When the rupture goes through B/B interface, the field offsets are systematically larger than the optical offsets (mean difference of -28 cm). When the rupture goes through B/S interface, the field offsets

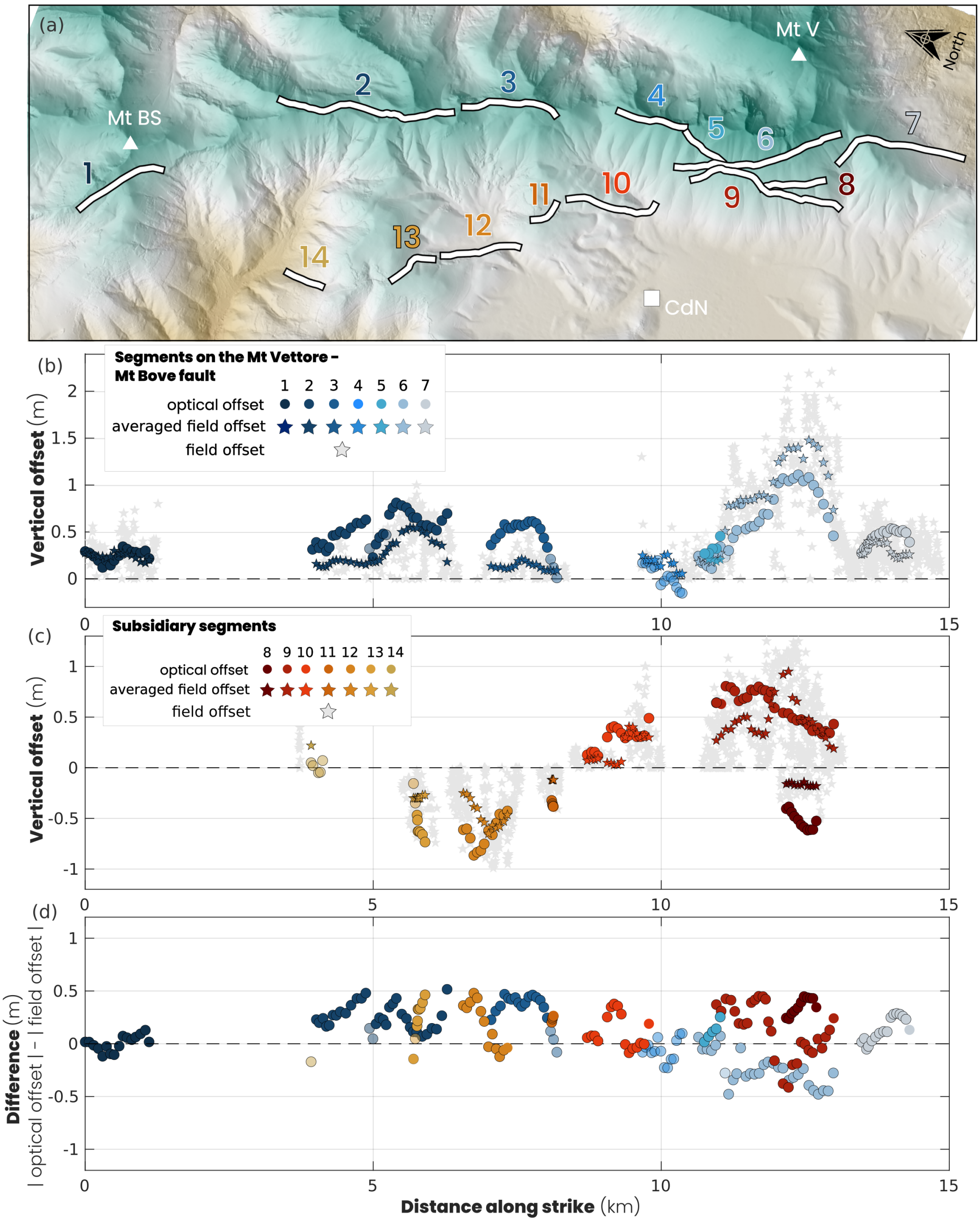

**Figure 3.** Comparison of optical and field offsets. (a) Shaded DEM showing the 14 rupture segments mapped from the 3D displacement field. The segments numbers are indicated and colored according to their location. Blueish segments denote the segments located on the main Mte Vettore-Mte Bove fault and reddish segments denote the subsidiary segments located within the hanging-wall of the main fault. Mt BS and Mt V locate the Monte Bove South and the Mont Vettore respectively. CdN locates the town of Castelluccio di Norcia. (b) Vertical optical and field offsets (throw) measured along the segments of the Mt Vettore-Mt Bove main fault (c) Vertical optical and field offsets measured along the subsidiary segments within the hanging-wall of the main fault. Negative values denote offset on antithetic fault segments (i.e. NE dipping). (d) Difference between the optical and averaged field offsets. On figures b-d, optical offsets plotted with a lower opacity level denote the offsets having a confidence level of 3 (low confidence level).

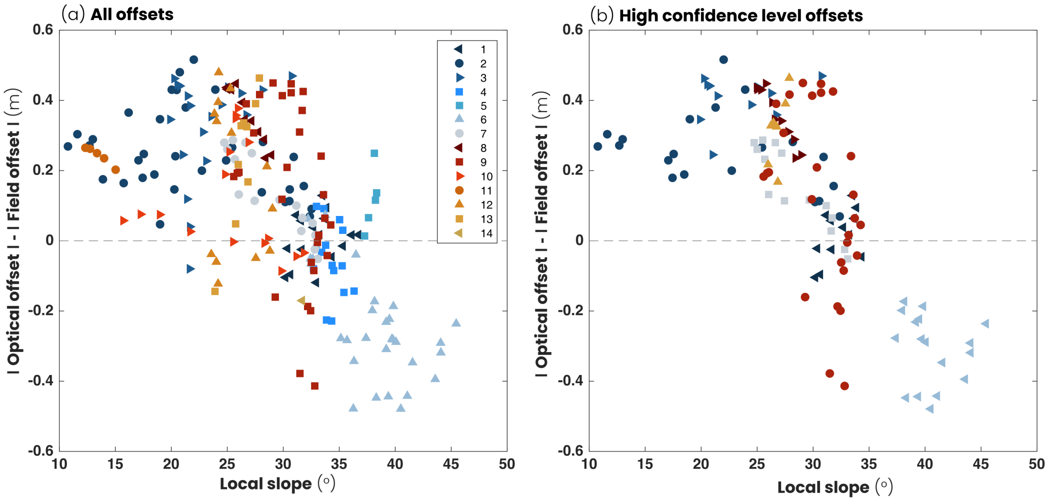

**Figure 4.** Difference between optical and field offset as a function of the local topographic slope for (a) all data points (b) data points having a confidence level of 1 (high confidence level, see main text for details).

are on average larger than the optical offsets (mean difference of -13 cm), although some data points have positive difference (8 over 34 data points). OFD (i.e. when optical offsets are larger than field offsets) is mainly found when the rupture goes through unconsolidated materials and soils, with an average difference of 20 cm. We note that the B/B and B/S categories are under-represented, as the majority of data points (82%) belongs to the B/S category (Figures 5 and S14).

### 4.2 Fault Slip Model & Shallow Slip Deficit

Our preferred slip model is shown in Figure 6. The slip distribution on the main fault shows a main slip patch located between 2 km and 7 km depth (Figure 6a). The patch is composed of two zones of maximum slip where the slip reaches 3.5 m, one at 2.8 km depth and a larger one, southward, at 4.6 km depth. Above 2 km depth, the slip distribution is very heterogeneous with several sub-patches of slip disconnected from each others with a maximum amplitude of 1.3 m. This fault slip distribution roughness that we infer at shallow depths may also exist at depth, but our data (located only at the surface) are not able to resolve it. The main slip patch at depth and the sub-patches of slip are separated by a pronounced slip gap located at 1.5 km depth. The gap is also visible on the distribution of cumulative slip with depth (Figure 6e). On the secondary segments, the slip amplitude is lower and reaches $\sim$1 m at the surface (Figure 6b,c). The slip model leads to a geodetic moment of $1.01 \times 10^{19}$ N.m (Mw 6.6) and a normal-slip pseudo-focal mechanism consistent with seismological estimates (Figure 6d). The distribution of cumulative slip with depth shows a very pronounced SSD of 72% ($\sim$70 cm). Note that the SSD is 10% larger when the secondary segments are not taken into account, illustrating the importance of including secondary segments to estimate the slip budget of a fault system.

Figures 7, 8, and 9 compare the observations with the model predictions for the optical, InSAR, and GPS data, respectively. The optical data are well reproduced by the slip model with a RMS of 0.17 m, 0.13 m, and 0.24 m for the EW, NS, and vertical components respectively. The residuals display only short length scale differences, not correlated with the fault trace, suggesting that they are not from tectonic origins. The T92D, T196A, and T197A interferograms have a very satisfactory RMS (0.05 m, 0.04 m, and 0.04 m,

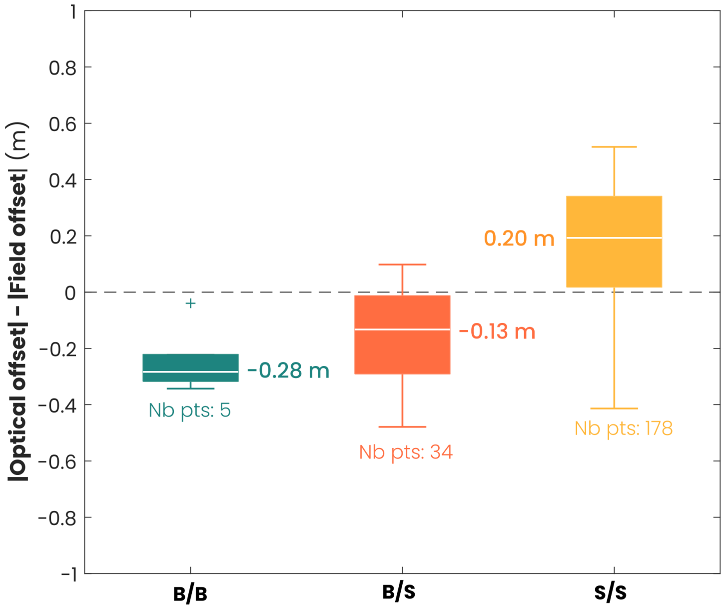

**Figure 5.** Impact of the local subsurface lithology on the difference between optical and field offset. Each box shows the statistics of the difference between optical and field offsets depending on whether the fault goes through (i) bedrock on both sides of the fault (B/B), (ii) bedrock on one side and unconsolidated materials and soils on the other (B/S), or (iii) through unconsolidated materials and soils on both sides of the fault (S/S). For each case, the white line indicates the mean, the bottom and top edges of the box indicate the 25th and 75th percentiles, and the vertical lines extend to the 2nd and 98th percentiles. Outliers are marked with the '+' symbol. The mean difference and the number of data points are written next to and below each box, respectively.

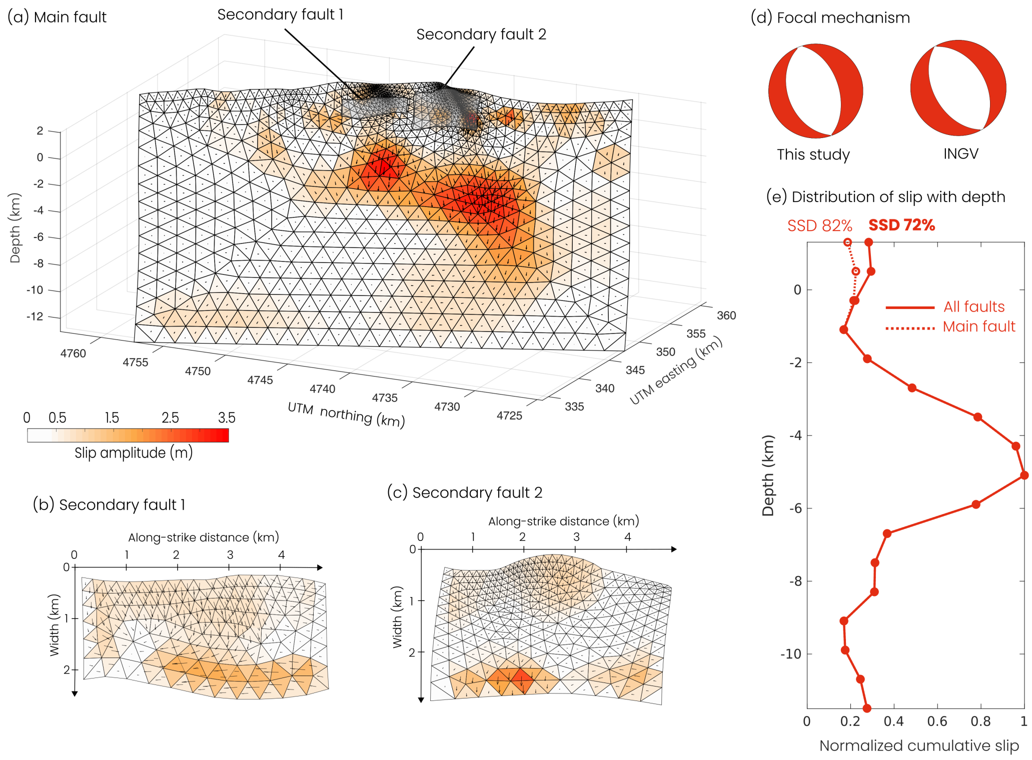

**Figure 6.** Preferred slip model and distribution of slip with depth. Slip amplitude and rake on (a) the main fault (b) the antithetic secondary fault (secondary fault 1) and (c) the synthetic secondary fault (secondary fault 2). The shaded gray areas on panel (a) indicate the location of the secondary faults. (c) Comparison of the pseudo focal mechanism computed from the slip model (this study) with the INGV focal mechanism. (e) Normalized cumulative slip with depth computed for the main fault only (red dotted line) and for the three segments (red line). The percentage of Shallow Slip Deficit (SSD) for both cases is indicated on top of the figure.

respectively). The main coseismic signal is very well reproduced by the model. The residuals consist of small amplitude signals correlated over tens of kilometers that may represent atmospheric noise. Moreover, we do not observe systematic larger residuals near the fault, indicating that the optical and InSAR data are consistent. Concerning the GPS data, the RMS for the EW, NS and vertical components are 0.02 m, 0.01 m, 0.006 m, respectively. The vertical component of the near-fault stations is very well reproduced by the model while the fit to the horizontal component of some stations show larger misfits, either concerning the direction of horizontal displacement (e.g. station CAMP) or the amplitude (e.g. station 1322).

As illustrated by the sensitivity distribution (Figures S8–9), optical data play a critical role in constraining both the distribution and amplitude of slip, not only at the surface but also down to $\sim$ 7 km depth (Figure S8). This is further evidenced by an alternative slip model derived only from InSAR data, which shows notable differences in both the shape and amplitude of slip at the surface and at depth (Figure S15).

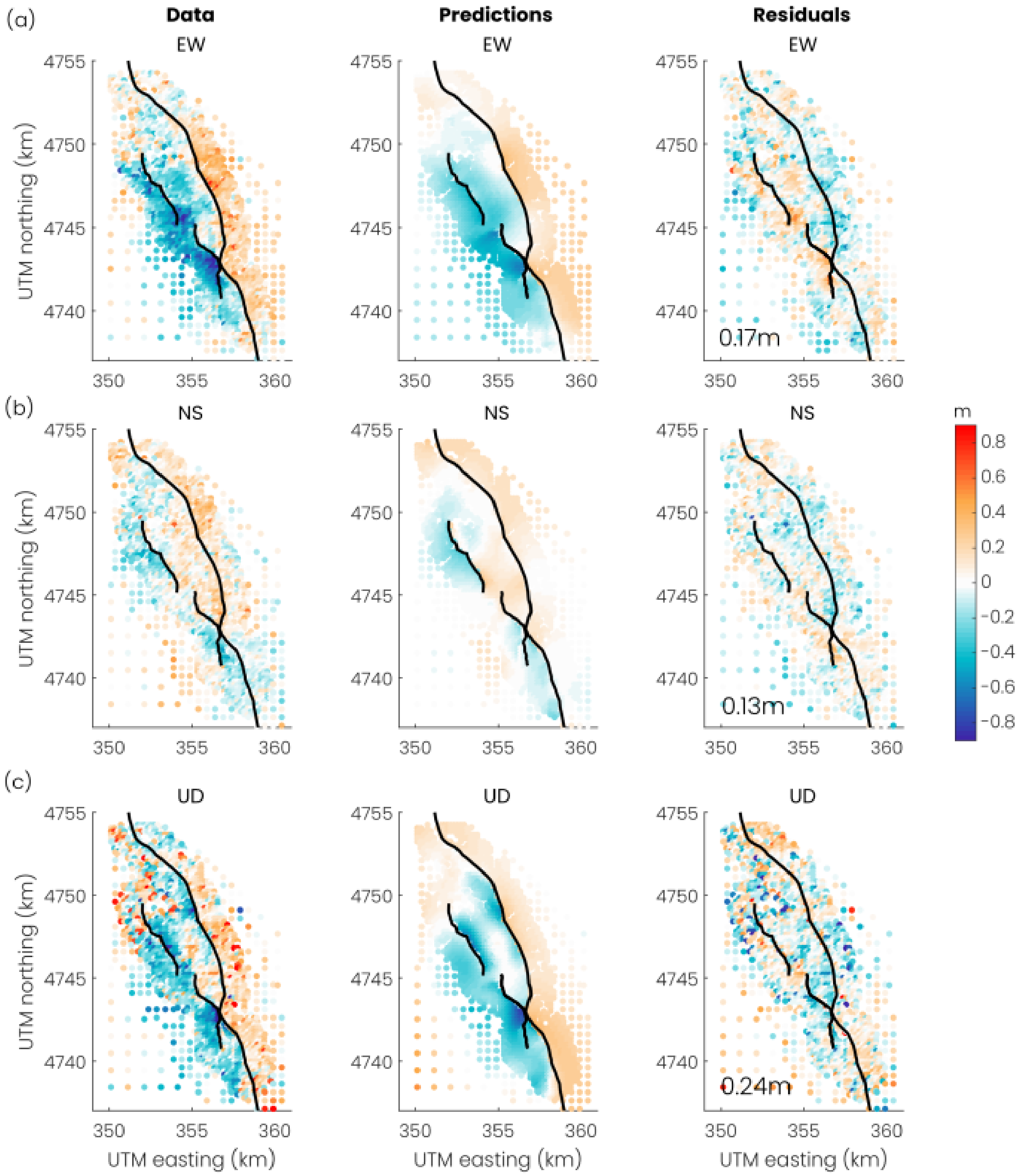

**Figure 7.** Subsampled optical data (left), model predictions (middle), and residuals (right) for the (a) EW (b) NS and (c) UD components of displacement. The black lines show the surface traces of the three modeled segments. For each residual map, the RMS value is shown.

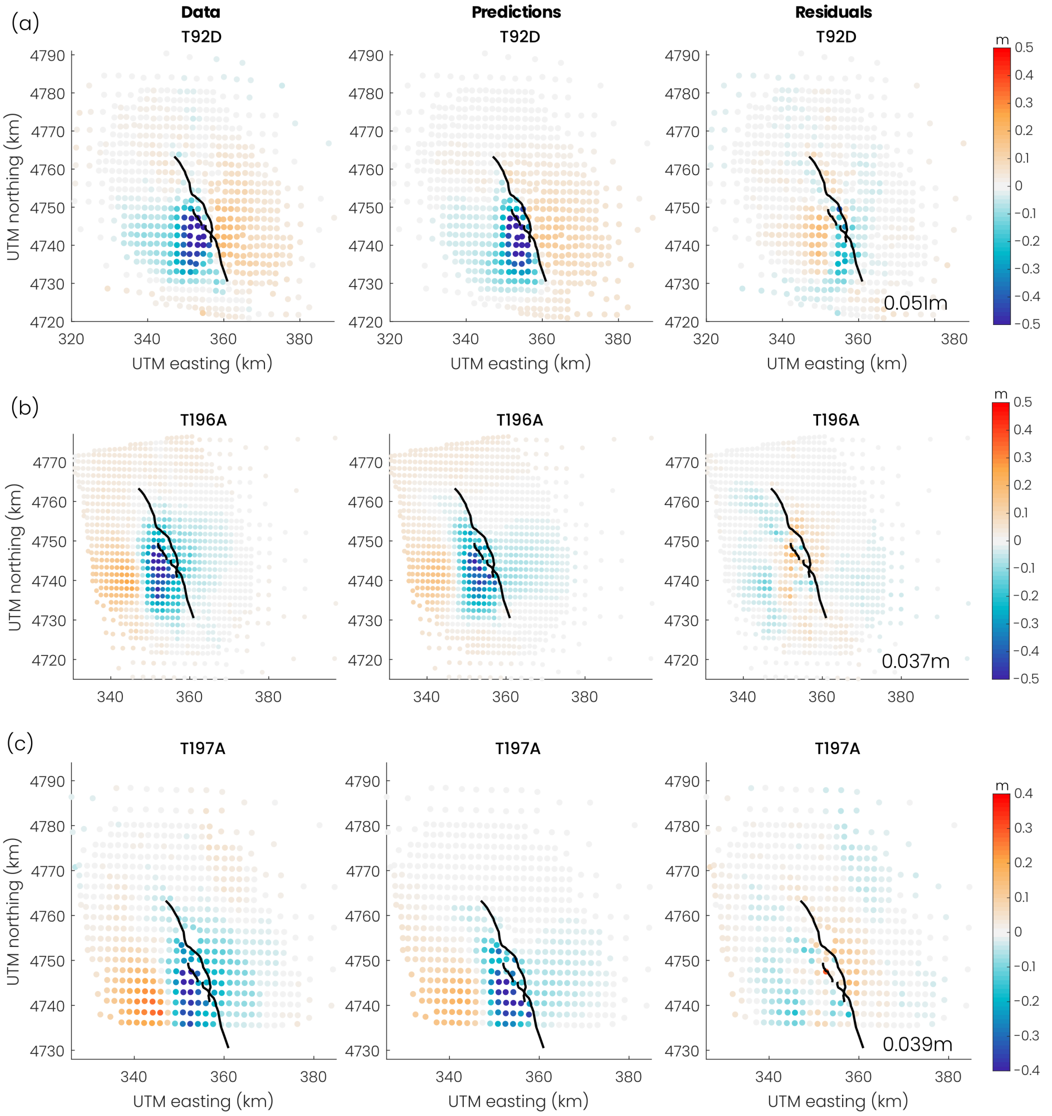

**Figure 8.** Subsampled LOS displacements (left), model predictions (middle), and residuals (right) for the (a) T92 descending (b) T196 ascending and (c) T197 ascending interferograms. The black lines show the surface traces of the three modeled segments.For each residual map, the RMS value is shown.

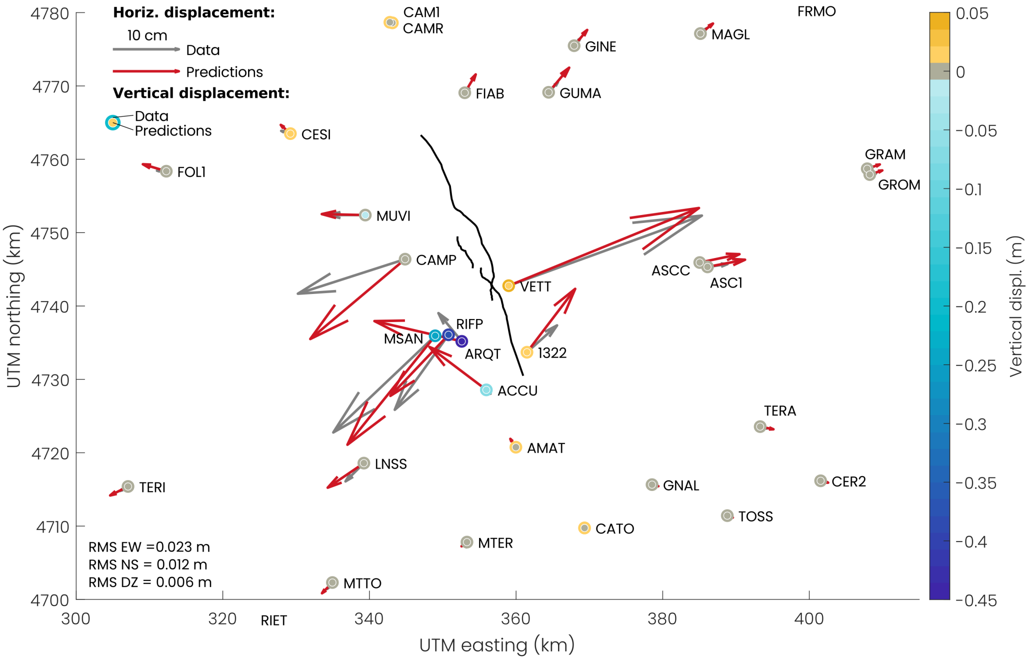

**Figure 9.** Data and model predictions for the GPS data. The gray and red arrows show the observed and predicted horizontal displacements, respectively. The outer and inner colored circles show the observed and predicted vertical displacements, respectively. The black lines show the surface traces of the three modeled segments.

# 5 Discussion

## 5.1 Factors Controlling Off-Fault Deformation

While a large body of literature has been published on measuring off-fault deformation and understanding its controlling factors in strike-slip earthquakes (Milliner et al., 2015, 2016; Zinke et al., 2014; Vallage et al., 2015; Gold et al., 2015; Scott et al., 2018b; Zinke et al., 2019; Barnhart et al., 2020; Antoine et al., 2022; Li, Li, Shan, & Zhang, 2023; Gaudreau et al., 2023; Li, Li, Hollingsworth, et al., 2023; Liu-Zeng et al., 2024; Liu et al., 2025), only two studies, to the best of our knowledge, have focused on normal events. Andreuttiova et al. (2022) studied the 1959 Mw∼7.2 Hebgen Lake earthquake from high-resolution historical aerial images and estimated ∼50% of OFD, with larger values where the local fault strike deviates from the average fault strike. Wedmore et al. (2019) estimated the amount of OFD along a 150 m long portion of the Norcia rupture using Using Terrestrial Laser Scanning (TLS) data. They found that 50% of the horizontal deformation was distributed within 8 m of the fault while the vertical component exhibits a smaller amount of OFD (16%) within a narrower zone (4 m). They suggest that this partitioning of displacement could be attributed either to a steepening of the fault dip angle toward the surface or to the opening of a network of shallow fractures.

Here, we estimate 46% (24.5 cm) of OFD on average for the entire rupture. The factors influencing the amount of OFD from one earthquake rupture to another are not yet fully understood. However, fault zone maturity is believed to be a key factor, with slip on mature faults being more localized (smaller OFD) than on immature faults (Dolan & Haravitch, 2014; Zinke et al., 2014, 2019). According to the fault maturity criterion of Manighetti et al. (2007), the Monte-Vettore-Monte-Bove fault system on which the Norcia earthquake occurred is an immature fault (e.g. cumulative slip of <50 m, maximum vertical long-term slip rate of 1.2±0.4mm/y, age < 250 kyr, fault length ∼ 30 km; Puliti et al., 2020; Pousse-Beltran et al., 2022). The 46% of OFD we estimate is thus consistent with the maturity level of the Monte-Vettore-Monte-Bove (Dolan & Haravitch, 2014).

The amount of OFD is variable along the Norcia rupture, with values ranging from 2% to 93%. Comparison of the percentage of OFD against the local topographic slope and type of near surface materials show that the degree of localization of the deformation decreases with the topographic slope (Figure 4) and when the rupture goes through unconsolidated materials and soils (Figure 5). Interestingly, a correlation between OFD and topographic slope was previously observed, albeit positive (higher OFD in steeper areas), for the Kaikoura earthquake (Zinke et al., 2019). Several processes could induce a correlation between OFD and the topographic slope. Firstly, amplification of the seismic waves by the topography (e.g. Boore, 1972; Bouchon et al., 1996) could result in the creation (or reactivation) of new fractures in the host rocks, leading to a positive correlation between OFD and topography slope (e.g. Zinke et al., 2019). Alternatively, topography slope might act as a first-order proxy for the sub-surface rock lithology, with weak sediments located in flat areas (e.g. basins) while steep slopes are made of strong, competent material; leading to a negative correlation between OFD and topographic slope, as observed here. We also infer larger values of OFD where the rupture goes trough unconsolidated material and soils (20 cm) compared to when the rupture goes through bedrock (no OFD) (Figure 5) suggesting that the positive correlation observed between the topographic slope and OFD reflects the impact of the subsurface materials on the localization of the deformation.

New evidence also suggests that the orientation of the fault segments with respect to the stress field could impact the degree of localization of the deformation, with higher degree of localization for well oriented segments (Liu-Zeng et al., 2024). The Norcia rupture features strong variations of strike (e.g. Figure 3), therefore we evaluate whether a correlation between the amount of OFD and the local fault azimuth exists (Figure 10). When all data points are plotted, no correlation is found between the local azimuth and the amount of OFD (Figure 10a). However, when the average OFD by segment is considered, we find that two of the three segments with the lowest OFD values (≤10%) are well oriented segments (i.e. whose azimuth is parallel to SHmax; segments 1 and 6; Figure 10b) whereas all segments featuring high OFD values (≥40%, segments 2, 3, 10, and 13) are all not well oriented segments (azimuth outside the SHmax range of the Norcia area; Figure 10b). Taken together, these observations suggest that the orientation of the segments with respect to the stress field could have played a role, albeit weak, on the degree of localization of the deformation during the Norcia earthquake.

### 5.2 Link between Shallow Slip Deficit and Off-Fault Deformation

Understanding how surface offsets relate to slip at depth is crucial for accurately interpreting long-term cumulative fault offsets and, in turn, for making reliable seismic hazard assessments. The deficit of shallow slip inferred from inversion of high-resolution geodetic data for moderate to large continental earthquakes (Fialko et al., 2005), suggests that long-term slip-rates - deduced from offset geological markers - could be underestimated if they do not take into account the distributed off-fault component, in particular for immature faults (Dolan & Haravitch, 2014; Milliner et al., 2025) For these reasons, understanding the origin of the deficit of shallow slip, and its link with the degree of localization of the deformation at the surface is of primary importance. Several hypotheses have been proposed to explain SSD. Firstly, SSD could be accommodated by postseismic or interseismic aseismic shallow creep. This hypothesis is supported by the velocity strengthening behavior of the shallow part of the crust (Dieterich, 1978; Marone et al., 1991; Rice, 1993). However, postseismic shallow creep is generally insufficient to compensate for the deficit of slip (e.g. Pousse-Beltran et al., 2020) while shallow interseismic creep has only been documented on a limited number of faults (e.g. Kaneko et al., 2013; Pousse Beltran et al., 2016). More-

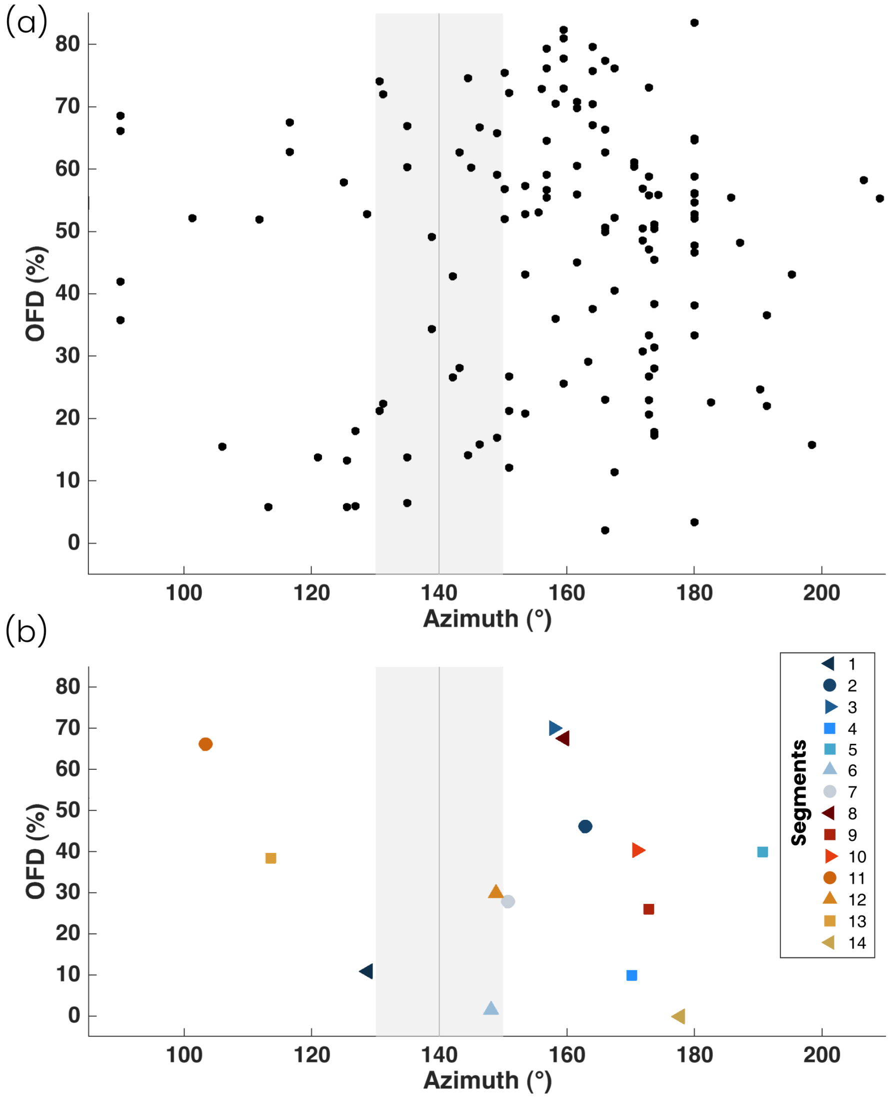

**Figure 10.** (a) OFD (%) as a function of the local fault azimuth (°) (a) for all data points and (b) averaged over each segment. The gray thin line represents the average SHmax in the Norcia region while the shaded area delineates the 25th-75th percentile SHmax range. In an Andersonian stress regime for normal faulting, the azimuth of an optimally-oriented normal fault is parallel to SHmax.

over, interseismic creep is typically observed for mature faults (e.g. Karabacak et al., 2011; Kaneko et al., 2013; Lindsey et al., 2014; Rousset et al., 2016) for which we expect SSD to be minimal (Dolan & Haravitch, 2014). It has also been shown that a part of SSD could be a modeling artifact due to either an imperfect representation of the medium when inverting for the fault slip, data noise, a lack of near-fault data coverage, biased near-fault data, or locally incorrect fault geometry (Kaneko & Fialko, 2011; X. Xu et al., 2016; Marchandon et al., 2021; Wang et al., 2024). Another hypothesis suggests that the shallow slip deficit (SSD) may be compensated by coseismic inelastic deformation occurring within the volume surrounding the fault (Fialko et al., 2005; Dolan & Haravitch, 2014). This idea is supported by dynamic rupture simulations for simple strike-slip faults incorporating elasto-plastic off-fault response (Kaneko & Fialko, 2011; Roten et al., 2017). These simulations demonstrate that the plastic response of the surrounding medium tends to lower or suppress (depending on the medium plastic strength) the slip at shallow depths (albeit only in the uppermost 300 m of the crust, Roten et al., 2017). This hypothesis, that inelastic deformation around the fault may compensate for the shallow slip deficit, is also supported by recent studies that found a correlation between optically-derived off-fault deformation and shallow slip deficit along the fault strike (Antoine et al., 2024; Liu et al., 2025). Here, we do not find any correlation between the amount of OFD estimated at the surface and the amount of SSD (Figure 11). The reason explaining this discrepancy might reside in the method used to estimate the off-fault deformation. The correlation between SSD and OFD is usually found in studies that measure kilometer-scale off-fault deformation by making the assumption that any gradient in fault-perpendicular surface displacement profiles reflects inelastic deformation. In contrast, the method used here, by differentiating field and optical offsets, measures off-fault deformation at a much smaller scale. The two methods might therefore be sensitive to distinct underlying processes, occurring over different spatial scales and depth ranges. Here, the lack of correlation between SSD and OFD along with the correlation between OFD and the type of sub-surface material suggest that the OFD we observe in this study results from the shallow soil response to coseismic rupture. Simulations that account for the mechanical behavior of different soil types (e.g. clay-like or sand-like) are needed to test this hypothesis and to fully understand how the very shallow subsurface affects the degree of deformation localization.

One central issue to understand the link between off-fault deformation and on-fault slip is our ability to untangle the respective contribution of inelastic and elastic processes in the observed surface displacements as both processes can produce similar surface deformation patterns (Nevitt et al., 2020; Hayek et al., 2024). A full understanding of the mechanical behavior of the shallow crust solely based on observations is therefore difficult. Systematic investigation of surface rupturing earthquakes using dynamic rupture simulations incorporating inelastic rheology (e.g. Hayek et al., 2024) can help decipher the underlying processes responsible of the near-fault surface displacement pattern. Ultimately, an inversion method incorporating elasto-plastic Green's functions would offer a unified approach to simultaneously resolve both elastic and inelastic processes.

## 6 Conclusion

We present the first analysis of on- and off-fault deformation for the 2016 Mw 6.5 Norcia, Italy, earthquake. We first measure the near-field 3D displacements of the Norcia event from the correlation of high-resolution stereo optical images. By comparing field and optically-derived fault offsets, we estimate 46% (26 cm) of off-fault deformation. Then, we extend our analysis to the slip at depth from a joint inversion of optical, InSAR, and GPS data. We use an inversion method that takes into account the medium complexities (non-planar multi-segmented fault geometry, topography, and 3D medium properties) in order to infer an unbiased slip distribution. Our slip model reveals a highly heterogeneous slip distribution, with a main slip patch at depth and several sub-patches of slip at the surface that are disconnected from the main patch by a distinct slip gap. The distribution of slip

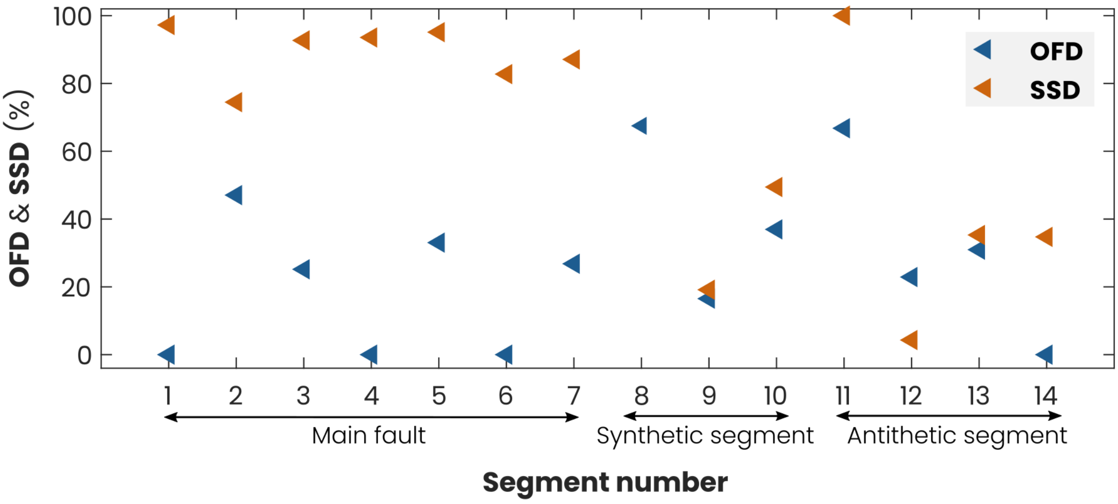

**Figure 11.** Comparison of the average amount of OFD (%) with the average amount of SSD(%) computed per segment, showing no correlation between the amount of OFD and the amount SSD. See Figure 3a for the location of the segments.

with depth shows a Shallow Slip Deficit (SSD) of 75%. We observe a positive correlation between the local topographic slope and the amount of OFD as well as lower OFD values when the rupture goes through unconsolidated materials and soils. We also found that the orientation of the fault segments within the regional stress field does not impact significantly the amount of OFD and that the along-strike variation of SSD does not correlate with the along-strike variation of OFD. Taken together, these results suggest that the off-fault deformation estimated in this study reflects surficial processes probably occurring in the first tens of meters depth (i.e. within the soil). We argue that inversion methods taking into account elasto-plastic rheologies are needed for a robust estimation of the distribution of slip with depth as well as for untangling the relative contribution of inelastic versus elastic processes within the shallow crust.

## Open Research Section

The InSAR and optical displacement fields, optical and mean field offsets (along with the type of interface and the local topographic slope at each offset location), and the slip model can be downloaded from the Zenodo repository available at `https://doi.org/10.5281/zenodo.16742625`. The Pleiades and Worldview satellite imagery were processed with the open source software packages Ames Stereo Pipeline (`https://github.com/NeoGeographyToolkit/StereoPipeline/`) and COSI-Corr (`https://github.com/SaifAati/Geospatial-COSICorr3D`). The ALOS-2 SAR images were processed with the GMTSAR processing chain (`https://github.com/gmtsar/gmtsar`). The GPS data were downloaded from the Rete Integrata Nazionale GPS (RING) website (`http://ring.gm.ingv.it`). We use the open-source software package Pylith available at `https://github.com/geodynamics/pylith`, to compute the Green's functions used in our inversion. The INGV focal mechanism for the Norcia earthquake plotted in Figure 5d is available at `https://terremoti.ingv.it/en/event/8863681#`.

## Acknowledgments

We thank Andrew Steele (Maxar) for assistance with WorldView data. The Pleiade data are from the DINAMIS system, funded by CNES, CNRS, IGN, IRD, INRAE and CIRAD.

JH acknowledges support from ANR (ANR-22-CE01-0028). MM and AAG were supported by Horizon Europe (DT-GEO, grant no. 101058129; and Geo-INQUIRE). Geo-INQUIRE is funded by the European Commission under project number 101058518 within the HORIZON-INFRA-2021-SERV-01 call. AAG acknowledges additional support from Horizon Europe (ChEESE-2P, grant no. 101093038), the National Science Foundation (grant nos. EAR-2225286, EAR-2121568, OAC-2311208 and OAC-2311206) and the National Aeronautics and Space Administration (grant no. 80NSSC20K0495). This research was partly supported by the CNES (French spatial agency) through the funding of Mathilde Marchandon's post-doc and by ISTerre through the funding of LM's internship. Computing resources were provided by the Institute of Geophysics of LMU Munich (Oeser et al., 2006).

## References

Aagaard, B. T., Knepley, M. G., & Williams, C. A. (2013). A domain decomposition approach to implementing fault slip in finite-element models of quasi-static and dynamic crustal deformation. *Journal of Geophysical Research: Solid Earth*, *118*(6), 3059–3079.

Ajorlou, N., Hollingsworth, J., Mousavi, Z., Ghods, A., & Masoumi, Z. (2021). Characterizing near-field surface deformation in the 1990 rudbar earthquake (iran) using optical image correlation. *Geochemistry, Geophysics, Geosystems*, *22*(6), e2021GC009704.

Andreuttiova, L., Hollingsworth, J., Vermeesch, P., Mitchell, T. M., & Bergman, E. (2022). Revisiting the 1959 hebgen lake earthquake using optical image correlation; new constraints on near-field 3d ground displacement. *Geophysical Research Letters*, *49*(16), e2022GL098666.

Andrews, D. (2005). Rupture dynamics with energy loss outside the slip zone. *Journal of Geophysical Research: Solid Earth*, *110*(B1).

Antoine, S. L., Klinger, Y., Delorme, A., & Gold, R. D. (2022). Off-fault deformation in regions of complex fault geometries: The 2013, mw7. 7, baluchistan rupture (pakistan). *Journal of Geophysical Research: Solid Earth*, *127*(11), e2022JB024480.

Antoine, S. L., Klinger, Y., Delorme, A., Wang, K., Bürgmann, R., & Gold, R. D. (2021). Diffuse deformation and surface faulting distribution from submetric image correlation along the 2019 ridgecrest, california, ruptures. *Bulletin of the Seismological Society of America*, *111*(5), 2275–2302.

Antoine, S. L., Klinger, Y., Wang, K., & Bürgmann, R. (2024). Coseismic shallow slip deficit accounted for by diffuse off-fault deformation. *Geophysical Research Letters*, *51*(24), e2024GL110798.

Avouac, J.-p., & Leprince, S. (2015). *Geodetic Imaging using optical systems* (Vol. 3). Elsevier B.V. Retrieved from `http://dx.doi.org/10.1016/B978-0-444-53802-4.00067-1` doi: 10.1016/B978-0-444-53802-4.00067-1

Ayoub, F., Leprince, S., & Keene, L. (2017). User's guide to cosi-corr co-registration of optically sensed images and correlation. *California Institute of Technology: Pasadena, CA, USA*, *38*, 49s.

Barnhart, W. D., Gold, R. D., & Hollingsworth, J. (2020). Localized fault-zone dilatancy and surface inelasticity of the 2019 ridgecrest earthquakes. *Nature Geoscience*, *13*(10), 699–704.

Boore, D. M. (1972). A note on the effect of simple topography on seismic sh waves. *Bulletin of the seismological Society of America*, *62*(1), 275–284.

Bouchon, M., Schultz, C. A., & Toksöz, M. N. (1996). Effect of three-dimensional topography on seismic motion. *Journal of Geophysical Research: Solid Earth*, *101*(B3), 5835–5846.

Brozzetti, F., Boncio, P., Cirillo, D., Ferrarini, F., De Nardis, R., Testa, A., ... Lavecchia, G. (2019). High-resolution field mapping and analysis of the august–october 2016 coseismic surface faulting (central italy earthquakes): Slip distribution, parameterization, and comparison with global earthquakes. *Tectonics*, *38*(2), 417–439.

Carboni, F., Porreca, M., Valerio, E., Mariarosaria, M., De Luca, C., Azzaro, S., ... Barchi,

M. R. (2022). Surface ruptures and off-fault deformation of the october 2016 central italy earthquakes from dinsar data. *Scientific Reports*, *12*(1), 3172.

Cello, G., Mazzoli, S., Tondi, E., & Turco, E. (1997). Active tectonics in the central apennines and possible implications for seismic hazard analysis in peninsular italy. *Tectonophysics*, *272*(1), 43–68.

Cheloni, D., De Novellis, V., Albano, M., Antonioli, A., Anzidei, M., Atzori, S., … others (2017). Geodetic model of the 2016 central italy earthquake sequence inferred from insar and gps data. *Geophysical Research Letters*, *44*(13), 6778–6787.

Chiarabba, C., De Gori, P., Cattaneo, M., Spallarossa, D., & Segou, M. (2018). Faults geometry and the role of fluids in the 2016–2017 central italy seismic sequence. *Geophysical Research Letters*, *45*(14), 6963–6971.

Chiaraluce, L., Di Stefano, R., Tinti, E., Scognamiglio, L., Michele, M., Casarotti, E., … others (2017). The 2016 central italy seismic sequence: A first look at the mainshocks, aftershocks, and source models. *Seismological Research Letters*, *88*(3), 757–771.

Chiaraluce, L., Stefano, R. D., Tinti, E., Scognamiglio, L., Michele, M., Cattaneo, M., … Marzorati, S. (2017). The 2016 Central Italy Seismic Sequence: A First Look at the Mainshocks, Aftershocks, and Source Models. *Seismological research letters*, *88*(3), 1–15. doi: 10.1785/0220160221

Civico, R., Pucci, S., Villani, F., Pizzimenti, L., De Martini, P. M., Nappi, R., & Group, O. E. W. (2018). Surface ruptures following the 30 october 2016 m w 6.5 norcia earthquake, central italy. *Journal of Maps*, *14*(2), 151–160.

Coleman, T. F., & Li, Y. (1996). A reflective newton method for minimizing a quadratic function subject to bounds on some of the variables. *SIAM Journal on Optimization*, *6*(4), 1040–1058.

Delorme, A., Grandin, R., Klinger, Y., Pierrot-Deseilligny, M., Feuillet, N., Jacques, E., … Morishita, Y. (2020). Complex deformation at shallow depth during the 30 october 2016 mw6. 5 norcia earthquake: interference between tectonic and gravity processes? *Tectonics*, *39*(2), e2019TC005596.

Dieterich, J. H. (1978). Time-dependent friction and the mechanics of stick-slip. *Pure and applied geophysics*, *116*, 790–806.

Dolan, J. F., & Haravitch, B. D. (2014). How well do surface slip measurements track slip at depth in large strike-slip earthquakes? The importance of fault structural maturity in controlling on-fault slip versus off-fault surface deformation. *Earth and Planetary Science Letters*, *388*, 38–47. Retrieved from `http://dx.doi.org/10.1016/j.epsl.2013.11.043` doi: 10.1016/j.epsl.2013.11.043

Falcucci, E., Gori, S., Bignami, C., Pietrantonio, G., Melini, D., Moro, M., … Galadini, F. (2018). The campotosto seismic gap in between the 2009 and 2016–2017 seismic sequences of central italy and the role of inherited lithospheric faults in regional seismotectonic settings. *Tectonics*, *37*(8), 2425–2445.

Farr, T. G., Rosen, P. A., Caro, E., Crippen, R., Duren, R., Hensley, S., … others (2007). The shuttle radar topography mission. *Reviews of geophysics*, *45*(2).

Fialko, Y. (2004). Temperature fields generated by the elastodynamic propagation of shear cracks in the Earth. *Journal of Geophysical Research*, *109*, 0–13. doi: 10.1029/2003JB002497

Fialko, Y., Sandwell, D., Simons, M., & Rosen, P. (2005). Three-dimensional deformation caused by the Bam, Iran, earthquake and the origin of shallow slip deficit. *Nature*, *435*, 295–299. doi: 10.1038/nature03425

Gabriel, A.-A., Ampuero, J.-P., Dalguer, L., & Mai, P. M. (2013). Source properties of dynamic rupture pulses with off-fault plasticity. *Journal of Geophysical Research: Solid Earth*, *118*(8), 4117–4126.

Galadini, F., & Galli, P. (2000). Active tectonics in the central apennines (italy)–input data for seismic hazard assessment. *Natural Hazards*, *22*, 225–268.

Gaudreau, E., Hollingsworth, J., Nissen, E., & Funning, G. (2023). Complex 3-d surface deformation in the 1971 san fernando, california earthquake reveals static and dynamic controls on off-fault deformation. *Journal of Geophysical Research: Solid*

*Earth*, *128* (3), e2022JB024985.

Gold, R. D., Reitman, N. G., Briggs, R. W., Barnhart, W. D., Hayes, G. P., & Wilson, E. (2015). On-and off-fault deformation associated with the september 2013 mw 7.7 balochistan earthquake: Implications for geologic slip rate measurements. *Tectonophysics*, *660* , 65–78.

Goldstein, R. M., Zebker, H. A., & Werner, C. L. (1988). Satellite radar interferometry: Two-dimensional phase unwrapping. *Radio science*, *23* (4), 713–720.

Hayek, J. N., Marchandon, M., Li, D., Pousse-Beltran, L., Hollingsworth, J., Li, T., & Gabriel, A.-A. (2024). Non-typical supershear rupture: Fault heterogeneity and segmentation govern unilateral supershear and cascading multi-fault rupture in the 2021 m w m_w 7.4 maduo earthquake. *Geophysical Research Letters*, *51* (20), e2024GL110128.

Hollingsworth, J., Lingling, Y., & Avouac, J.-p. (2017). Dynamically triggered slip on a splay fault in theMw 7.8, 2016 Kaikoura (New Zealand) earthquake. *Geophysical Research Letters*, 3517–3525. doi: 10.1002/2016GL072228

Jónsson, S., Zebker, H., Segall, P., & Amelung, F. (2002). Fault slip distribution of the 1999 m w 7.1 hector mine, california, earthquake, estimated from satellite radar and gps measurements. *Bulletin of the Seismological Society of America*, *92* (4), 1377–1389.

Kaneko, Y., & Fialko, Y. (2011). rupture simulations with elasto-plastic off-fault response. *Geophysical Journal International*, *186* , 1389–1403. doi: 10.1111/j.1365-246X.2011.05117.x

Kaneko, Y., Fialko, Y., Sandwell, D. T., Tong, X., & Furuya, M. (2013). Interseismic deformation and creep along the central section of the north anatolian fault (turkey): Insar observations and implications for rate-and-state friction properties. *Journal of Geophysical Research: Solid Earth*, *118* (1), 316–331.

Karabacak, V., Altunel, E., & Çakir, Z. (2011). Monitoring aseismic surface creep along the north anatolian fault (turkey) using ground-based lidar. *Earth and Planetary Science Letters*, *304* (1-2), 64–70.

Kuo, Y.-T., Wang, Y., Hollingsworth, J., Huang, S.-Y., Chuang, R. Y., Lu, C.-H., ... Chang, C.-P. (2019). Shallow fault rupture of the milun fault in the 2018 mw 6.4 hualien earthquake: A high-resolution approach from optical correlation of pléiades satellite imagery. *Seismological Research Letters*, *90* (1), 97–107.

Li, C., Li, T., Hollingsworth, J., Zhang, Y., Qian, L., & Shan, X. (2023). Strain threshold for the formation of coseismic surface rupture. *Geophysical Research Letters*, *50* (16), e2023GL103666.

Li, C., Li, T., Shan, X., & Zhang, G. (2023). Extremely large off-fault deformation during the 2021 m w 7.4 maduo, tibetan plateau, earthquake. *Seismological Society of America*, *94* (1), 39–51.

Lindsey, E. O., Fialko, Y., Bock, Y., Sandwell, D. T., & Bilham, R. (2014). Localized and distributed creep along the southern san andreas fault. *Journal of Geophysical Research: Solid Earth*, *119* (10), 7909–7922.

Liu, J., Jónsson, S., Li, X., Yao, W., & Klinger, Y. (2025). Extensive off-fault damage around the 2023 kahramanmaraş earthquake surface ruptures. *Nature Communications*, *16* (1), 1286.

Liu-Zeng, J., Liu, Z., Liu, X., Milliner, C., Rodriguez Padilla, A. M., Xu, S., ... others (2024). Fault orientation trumps fault maturity in controlling coseismic rupture characteristics of the 2021 maduo earthquake. *AGU Advances*, *5* (2), e2023AV001134.

Loveless, J. P., & Meade, B. J. (2011). Spatial correlation of interseismic coupling and coseismic rupture extent of the 2011 mw= 9.0 tohoku-oki earthquake. *Geophysical Research Letters*, *38* (17).

Manighetti, I., Campillo, M., Bouley, S., & Cotton, F. (2007). Earthquake scaling, fault segmentation, and structural maturity. *Earth and Planetary Science Letters*, *253* , 429–438. doi: 10.1016/j.epsl.2006.11.004

Marchandon, M., Hollingsworth, J., & Radiguet, M. (2021). Origin of the shallow slip deficit on a strike slip fault: Influence of elastic structure, topography, data coverage, and noise. *Earth and Planetary Science Letters*, *554*, 116696.

Marchandon, M., Vergnolle, M., Cavali, O., Sudhaus, H., & Hollingsworth, J. (2018). Earthquake sequence in the NE Lut, Iran : Observations from multiple space geodetic techniques. *Geophysical Journal International*, 1–37.

Marchandon, M., Wright, T. J., & Hollingsworth, J. (2022). Remote sensing of the earthquake deformation cycle. *Surface Displacement Measurement from Remote Sensing Images*, 191–246.

Marone, C. J., Scholtz, C., & Bilham, R. (1991). On the mechanics of earthquake afterslip. *Journal of Geophysical Research: Solid Earth*, *96*(B5), 8441–8452.

Milliner, C., Avouac, J.-P., Dolan, J., & Hollingsworth, J. (2025). Localization of inelastic strain with fault maturity and effects on earthquake characteristics. *Nature Geoscience*, 1–8.

Milliner, C., Dolan, J. F., Hollingsworth, J., Leprince, S., Ayoub, F., & Sammis, C. G. (2015). Quantifying near-field and off-fault deformation patterns of the 1992 mw 7.3 l anders earthquake. *Geochemistry, Geophysics, Geosystems*, *16*(5), 1577–1598.

Milliner, C., Sammis, C., Allam, A. A., Dolan, J. F., Hollingsworth, J., & Leprince, S. (2016). Resolving Fine-Scale Heterogeneity of Co-seismic Slip and the Relation to Fault Structure. *Scientific Reports*, *6*, 1–9. Retrieved from `http://dx.doi.org/10.1038/srep27201` doi: 10.1038/srep27201

Montagnon, T., Giffard-Roisin, S., Dalla Mura, M., Marchandon, M., Pathier, E., & Hollingsworth, J. (2024). Sub-pixel displacement estimation with deep learning: Application to optical satellite images containing sharp displacements. *Journal of Geophysical Research: Machine Learning and Computation*, *1*(4), e2024JH000174.

Nelson, M. R., & Jones, C. H. (1987). Paleomagnetism and crustal rotations along a shear zone, las vegas range, southern nevada. *Tectonics*, *6*(1), 13–33.

Nevitt, J. M., Brooks, B. A., Catchings, R. D., Goldman, M. R., Ericksen, T. L., & Glennie, C. L. (2020). Mechanics of near-field deformation during co-and post-seismic shallow fault slip. *Scientific Reports*, *10*(1), 5031.

Oeser, J., Bunge, H.-P., & Mohr, M. (2006). Cluster design in the earth sciences tethys. In *International conference on high performance computing and communications* (pp. 31–40).

Okada, Y. (1992). Internal deformation due to shear and tensite faults in a half-space. *Bulletin of Seismological Society of America*, 1018–1040.

Pizzi, A., Di Domenica, A., Gallovič, F., Luzi, L., & Puglia, R. (2017). Fault segmentation as constraint to the occurrence of the main shocks of the 2016 central italy seismic sequence. *Tectonics*, *36*(11), 2370–2387.

Pousse-Beltran, L., Benedetti, L., Fleury, J., Boncio, P., Guillou, V., Pace, B., … others (2022). 36cl exposure dating of glacial features to constrain the slip rate along the mt. vettore fault (central apennines, italy). *Geomorphology*, *412*, 108302.

Pousse-Beltran, L., Nissen, E., Bergman, E. A., Cambaz, M. D., Gaudreau, É., Karasözen, E., & Tan, F. (2020). The 2020 m w 6.8 elazığ (turkey) earthquake reveals rupture behavior of the east anatolian fault. *Geophysical Research Letters*, *47*(13), e2020GL088136.

Pousse Beltran, L., Pathier, E., Jouanne, F., Vassallo, R., Reinoza, C., Audemard, F., … Volat, M. (2016). Spatial and temporal variations in creep rate along the el pilar fault at the caribbean-south american plate boundary (venezuela), from insar. *Journal of Geophysical Research: Solid Earth*, *121*(11), 8276–8296.

Puliti, I., Pizzi, A., Benedetti, L., Di Domenica, A., & Fleury, J. (2020). Comparing slip distribution of an active fault system at various timescales: Insights for the evolution of the mt. vettore-mt. bove fault system in central apennines. *Tectonics*, *39*(9), e2020TC006200.

Rice, J. R. (1993). Spatio-temporal complexity of slip on a fault. *Journal of Geophysical Research: Solid Earth*, *98*(B6), 9885–9907.

Rockwell, T. K., Lindvall, S., Dawson, T., Langridge, R., Lettis, W., & Klinger, Y. (2002). Lateral offsets on surveyed cultural features resulting from the 1999 izmit and duzce earthquakes, turkey. *Bulletin of the Seismological Society of America*, *92*(1), 79–94.

Roten, D., Olsen, K., & Day, S. (2017). Off-fault deformations and shallow slip deficit from dynamic rupture simulations with fault zone plasticity. *Geophysical Research Letters*, *44*(15), 7733–7742.

Roten, D., Olsen, K., Day, S., & Cui, Y. (2018). Quantification of fault-zone plasticity effects with spontaneous rupture simulations. *Best practices in physics-based fault rupture models for seismic hazard assessment of nuclear installations*, 45–67.

Roten, D., Olsen, K., Day, S., Cui, Y., & Fäh, D. (2014). Expected seismic shaking in los angeles reduced by san andreas fault zone plasticity. *Geophysical Research Letters*, *41*(8), 2769–2777.

Rousset, B., Jolivet, R., Simons, M., Lasserre, C., Riel, B., Milillo, P., . . . Renard, F. (2016). An aseismic slip transient on the north anatolian fault. *Geophysical Research Letters*, *43*(7), 3254–3262.

Sandwell, D., Mellors, R., Tong, X., Wei, M., & Wessel, P. (2011). *Open radar interferometry software for mapping surface deformation.* Wiley Online Library.

Scognamiglio, L., Tinti, E., Casarotti, E., Pucci, S., Villani, F., Cocco, M., . . . Dreger, D. (2018). Complex fault geometry and rupture dynamics of the mw 6.5, 30 october 2016, central italy earthquake. *Journal of Geophysical Research: Solid Earth*, *123*(4), 2943–2964.

Scott, C. P., Arrowsmith, J. R., Nissen, E., Lajoie, L., Maruyama, T., & Chiba, T. (2018a). The m7 2016 kumamoto, japan, earthquake: 3-d deformation along the fault and within the damage zone constrained from differential lidar topography. *Journal of Geophysical Research: Solid Earth*, *123*(7), 6138–6155.

Scott, C. P., Arrowsmith, J. R., Nissen, E., Lajoie, L., Maruyama, T., & Chiba, T. (2018b). The m7 2016 kumamoto, japan, earthquake: 3-d deformation along the fault and within the damage zone constrained from differential lidar topography. *Journal of Geophysical Research: Solid Earth*, *123*(7), 6138–6155.

Shelef, E., & Oskin, M. (2010). Deformation processes adjacent to active faults: Examples from eastern california. *Journal of Geophysical Research: Solid Earth*, *115*(B5).

Socquet, A., Hollingsworth, J., Pathier, E., & Bouchon, M. (2019). Evidence of supershear during the 2018 magnitude 7.5 Palu earthquake from space geodesy. *Nature Geosciences*, *12*, 192–199.

Sudhaus, H., & Jonsson, S. (2011). Source model for the 1997 Zirkuh earthquake (Mw=7.2) in Iran derived from JERS and ERS InSAR observations. *Geophysical Journal International*, *185*(2), 676–692. doi: 10.1111/j.1365-246X.2011.04973.x

Tinti, E., Casarotti, E., Ulrich, T., Taufiqurrahman, T., Li, D., & Gabriel, A.-A. (2021). Constraining families of dynamic models using geological, geodetic and strong ground motion data: The mw 6.5, october 30th, 2016, norcia earthquake, italy. *Earth and Planetary Science Letters*, *576*, 117237.

Vallage, A., Klinger, Y., Grandin, R., & Bhat, H. S. (2015). Inelastic surface deformation during the 2013 Mw 7.7 Balochistan, Pakistan, earthquake. *Geology*, *43*(12), 1079–1082. doi: 10.1130/G37290.1

Villani, F., Civico, R., Pucci, S., Pizzimenti, L., Nappi, R., & De Martini, P. M. (2018). A database of the coseismic effects following the 30 october 2016 norcia earthquake in central italy. *Scientific data*, *5*(1), 1–11.

Waldhauser, F., Michele, M., Chiaraluce, L., Di Stefano, R., & Schaff, D. P. (2021). Fault planes, fault zone structure and detachment fragmentation resolved with high-precision aftershock locations of the 2016–2017 central italy sequence. *Geophysical Research Letters*, *48*(16), e2021GL092918.

Walters, R. J., Gregory, L. C., Wedmore, L. N., Craig, T. J., McCaffrey, K., Wilkinson, M., . . . others (2018). Dual control of fault intersections on stop-start rupture in the 2016 central italy seismic sequence. *Earth and Planetary Science Letters*, *500*, 1–14.

Wang, K., Xu, X., & Hu, Y. (2024). Kinematics of the 2023 kahramanmaraş earthquake doublet: Biased near-fault data and shallow slip deficit. *Seismol. Res. Lett. XX*, 1–10.

Wedmore, L., Gregory, L., McCaffrey, K., Goodall, H., & Walters, R. (2019). Partitioned off-fault deformation in the 2016 norcia earthquake captured by differential terrestrial laser scanning. *Geophysical Research Letters*, *46*(6), 3199–3205.

Xu, G., Xu, C., Wen, Y., & Jiang, G. (2017). Source parameters of the 2016–2017 central italy earthquake sequence from the sentinel-1, alos-2 and gps data. *Remote Sensing*, *9*(11), 1182.

Xu, X., Tong, X., Sandwell, D. T., Milliner, C., Dolan, J. F., Hollingsworth, J., … Ayoub, F. (2016). Refining the shallow slip deficit. *Geophysical Journal International*, *204*, 1867–1886. doi: 10.1093/gji/ggv563

Zinke, R., Hollingsworth, J., & Dolan, J. F. (2014). Surface slip and off-fault deformation patterns in the 2013MW 7.7 Balochistan, Pakistan earthquake: Implications for controls on the distribution of near-surface coseismic slip. *Geochemistry, Geophysics, Geosystems*, 5034–5050. doi: 10.1002/2014GC005538.Received

Zinke, R., Hollingsworth, J., Dolan, J. F., & Van Dissen, R. (2019). Three-dimensional surface deformation in the 2016 mw 7.8 kaikoura, new zealand, earthquake from optical image correlation: Implications for strain localization and long-term evolution of the pacific-australian plate boundary. *Geochemistry, Geophysics, Geosystems*, *20*(3), 1609–1628.

# Supporting Information for "Subsurface lithologic controls on off-fault deformation and multi-fault slip during the 2016 Mw 6.5 Norcia earthquake revealed by satellite geodesy"

Mathilde Marchandon[1], James Hollingsworth[2], Louise Maubant[3], Anne Socquet[2], Erwan Pathier[2], Mathilde Radiguet[2], and Alice-Agnes Gabriel[4,1]

[1]Department of Earth and Environmental Sciences, Ludwig-Maximillians-Universität München, Munich, Germany

[2]Univ. Grenoble Alpes, Univ. Savoie Mont Blanc, CNRS, IRD, Univ. Gustave Eiffel, ISTerre, Grenoble, France

[3]Earthquake Research Institute,The University of Tokyo, Tokyo, Japan

[4]Scripps Institution of Oceanography, UC San Diego, La Jolla, USA

## Contents of this file

1. Text S1
2. Figures S1 to S15
3. Tables S1 to S3

## Text S1: Removing the contribution of the Visso earthquake in the interferograms

Two of the three interferograms used in the inversion encompass both the Norcia earthquake and the Visso earthquake, that occurred 3 days before and 10 km north of the Norcia event. Therefore, as a preliminary step, we estimate and remove the contribution of the Visso earthquake from the concerned interferograms by performing a joint inversion for both the Visso and Norcia slip distribution. The principle of the method we use is similar to what has been done to jointly invert for co- and post-seismic on-fault slip

---

distribution (e.g. Ragon et al., 2019). In the inversion, we use the 115 GPS data points covering only the Norcia event, 128 GPS data points covering only the Visso earthquake (also downloaded from the Rete Integrata Nazionale GPS website, http://ring.gm.ingv.it), and the three ALOS-2 interferograms (Table S2).

Only the main fault is included in the modeling with a dip angle of 40°W. The fault is discretized with triangular subfaults ranging from ∼500 m at the surface to 1 km at depth. The Green's functions relating a unit of slip on each subfaults with the surface displacements are computed assuming an homogeneous elastic half-space (Meade, 2007). We solve for the strike and dip components of the slip on each subfault using a constrained linear least square inversion (Coleman & Li, 1992). We resolve the following system of equation:

$$\begin{bmatrix} \mathbf{d}_{GPS\_V} \\ \mathbf{d}_{GPS\_N} \\ \mathbf{d}_{Desc\_VN} \\ \mathbf{d}_{AscT197\_VN} \\ \mathbf{d}_{AscT196\_N} \end{bmatrix} = \begin{bmatrix} \mathbf{G}_{GPS\_V} & 0 \\ 0 & \mathbf{G}_{GPS\_N} \\ \mathbf{G}_{Desc\_V} & \mathbf{G}_{Desc\_N} \\ \mathbf{G}_{AscT197\_V} & \mathbf{G}_{AscT197\_N} \\ 0 & \mathbf{G}_{AscT196\_N} \end{bmatrix} \begin{bmatrix} \mathbf{m}_V \\ \mathbf{m}_N \end{bmatrix} \tag{1}$$

where $\mathbf{d}_{GPS\_V}$ and $\mathbf{d}_{GPS\_N}$ are the GPS data for the Visso and Norcia earthquakes, respectively. $\mathbf{d}_{Desc\_VN}$ and $\mathbf{d}_{AscT197\_VN}$ are the descending and ascending interferograms covering both the Visso and Norcia events, respectively. $\mathbf{d}_{AscT196\_N}$ is the ascending interferogram covering only the Norcia event. $\mathbf{G}_{Data\_Earthquake}$ is the matrix of Green's functions relating the data set *Data* to the model for the given *Earthquake*. For instance, $\mathbf{G}_{Desc\_N}$ is the matrix of Green's function relating the descending interferogram data points with the slip on the fault for the Norcia event, while $\mathbf{G}_{Desc\_V}$ is the matrix of Green's function relating the descending interferogram data points with the slip on the fault for the Visso event. In practice, these two matrices are exactly the same. $\mathbf{m}_V$ and $\mathbf{m}_N$ are the slip distributions for the Visso and Norcia earthquake, respectively.

The obtained slip models and the comparison of data with model predictions for the GPS and InSAR data are shown in Figures S5 and S6, respectively.

## References

Coleman, T. F., & Li, Y. (1992). A globally and quadratically convergent affine scaling method for linear 1 problems. *Mathematical Programming*, *56*(1-3), 189–222.

Meade, B. J. (2007). Algorithms for the calculation of exact displacements, strains, and stresses for triangular dislocation elements in a uniform elastic half space. *Computers & geosciences*, *33*(8), 1064–1075.

Ragon, T., Sladen, A., Bletery, Q., Vergnolle, M., Cavalié, O., Avallone, A., ... Delouis, B. (2019). Joint inversion of coseismic and early postseismic slip to optimize the information content in geodetic data: Application to the 2009 m w 6.3 l'aquila earthquake, central italy. *Journal of Geophysical Research: Solid Earth*, *124*(10), 10522–10543.

Villani, F., Civico, R., Pucci, S., Pizzimenti, L., Nappi, R., & De Martini, P. M. (2018). A database of the coseismic effects following the 30 october 2016 norcia earthquake in central italy. *Scientific data*, *5*(1), 1–11.

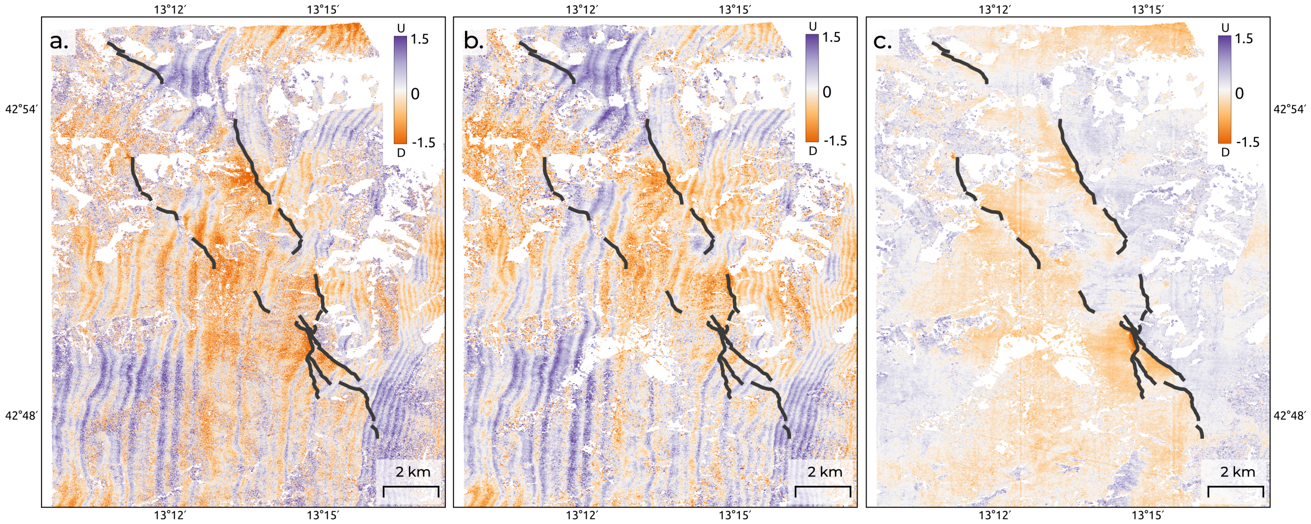

**Figure S1.** (a) Raw vertical coseismic displacement field obtained from the optical correlation of pre-earthquake Pleiade and post-earthquake Worldview images. The displacement field is corrupted with a strong aliasing signal due to the off-nadir incidence angle of the the post-earthquake Worldview images. (b) Aliasing component isolated from a post-earthquake Pleaides-Worlview correlation using Independent Component Analysis (FastICA) and used as template to corrected the raw coseismic displacement field. (c) Vertical coseismic displacement field corrected from the aliasing component. The spatial map of the aliasing component shown in (b) is multiplied by a coefficient allowing to minimize the standard deviation of the difference between this adjusted aliasing component and the raw coseismic displacement field (see method section in the main paper for details). The corrected coseismic displacement field is then obtained by removing the adjusted aliasing component from the raw coseismic displacement field.

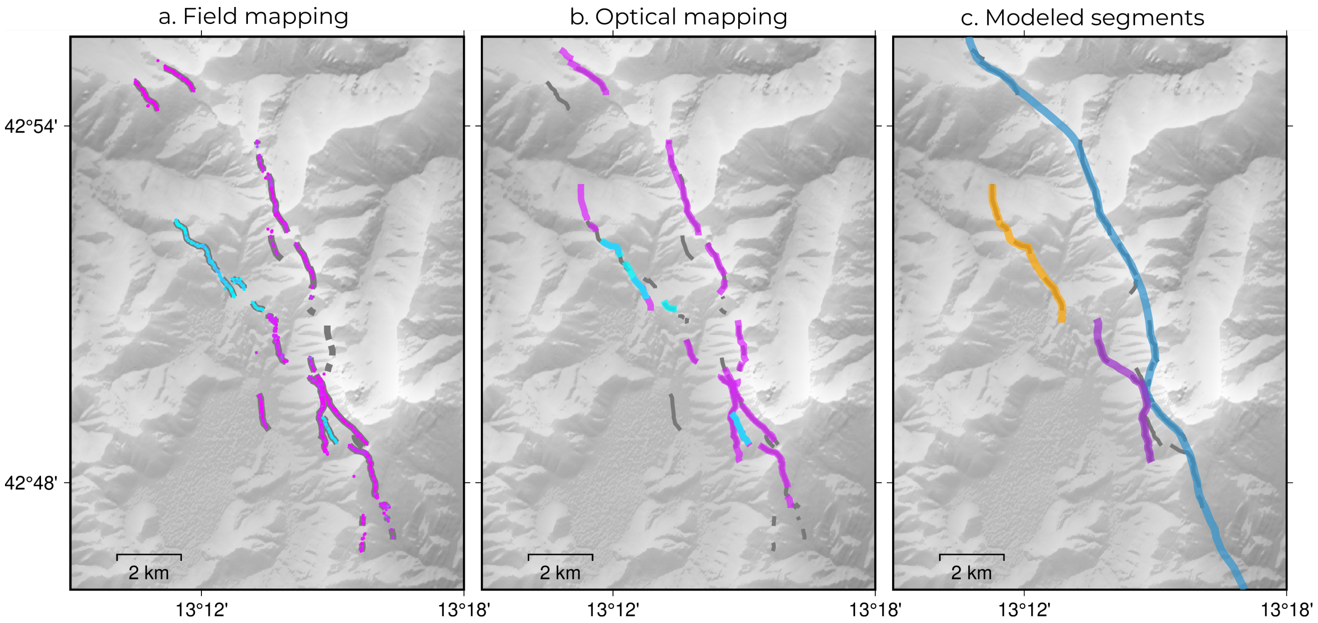

**Figure S2.** Field mapping, optical mapping and simplified modeled segments. (a) Surface rupture traces (gray) and dipping direction from field investigations (Villani et al., 2018). The purple color indicates a SW dipping surface rupture while the the blue color indicated a NE dipping surface rupture. (b) Surface rupture traces mapped from the optical correlation displacement field (blue and purple lines) plotted on top of the field mapping (gray line). As in (a), purple segments are SW dipping while blue segments are NE dipping. (c) Simplified fault segments used for the inversion (blue, purple, and orange lines) plotted on top of the optical surface rupture traces (gray lines). We modeled the complex and multi-segmented rupture with 3 segments: a SW dipping main segment (blue line) and two secondary segments, a NE dipping segment (orange line) antithetic to the main fault and a SW-dipping segment (dark purple line) synthetic to the main fault.

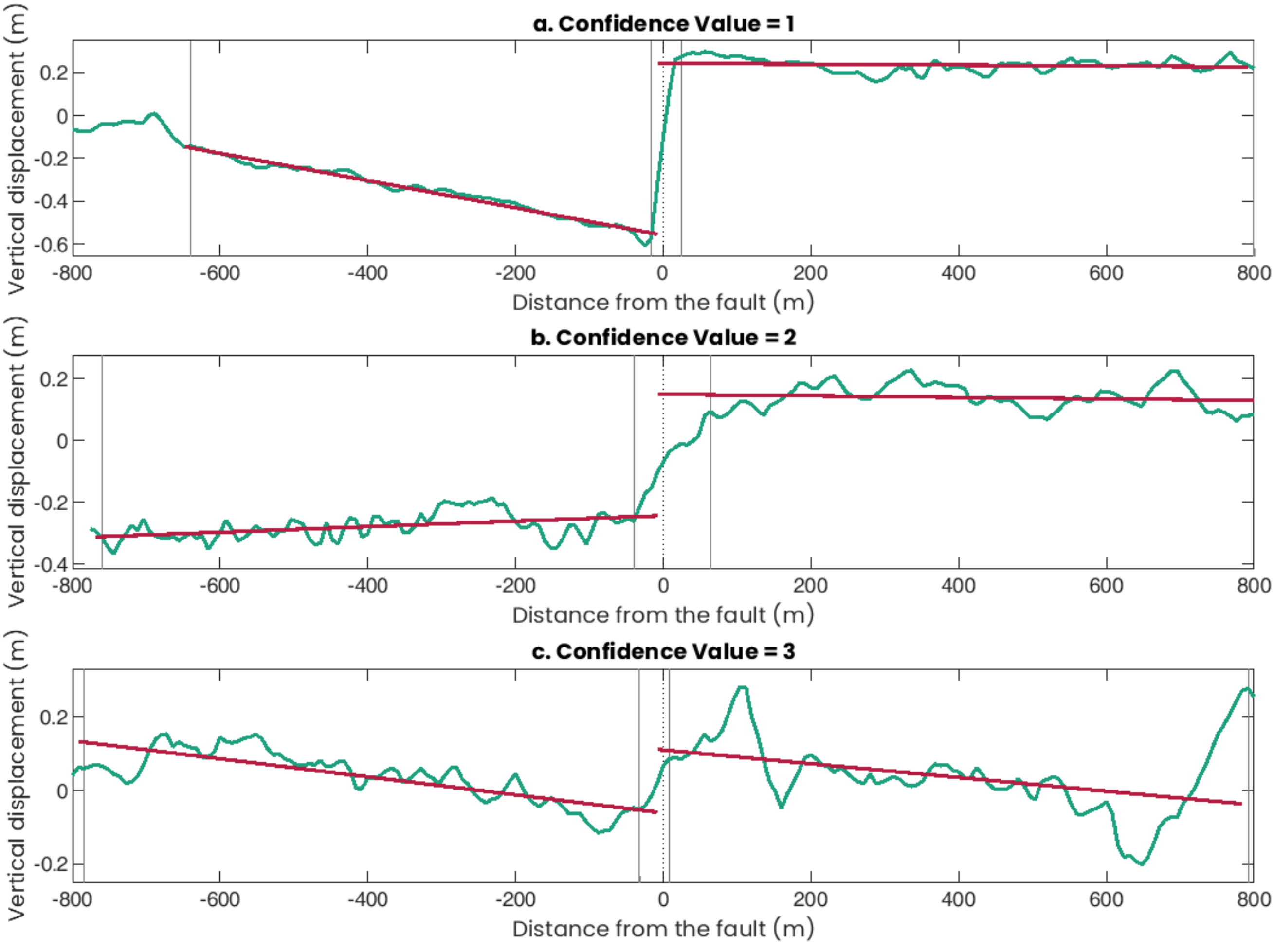

**Figure S3.** Examples of profile having a confidence value of (a) 1, (b) 2, and (c) 3. A confidence value of 1 means the offset can be measured unambiguously, a confidence value of 2 means the noise in the displacement profile can slightly impact the offset measurement, and a confidence value of 3 means that the noise in the displacement profile is such that the uncertainty of the measured offset is high. The gray dotted line shows the fault location, the red lines show the linear regressions applied to either side of the fault. The gray lines delineate the lateral extent used to compute the linear regression. The fault offset corresponds to the vertical distance between the red lines extrapolated on the fault.

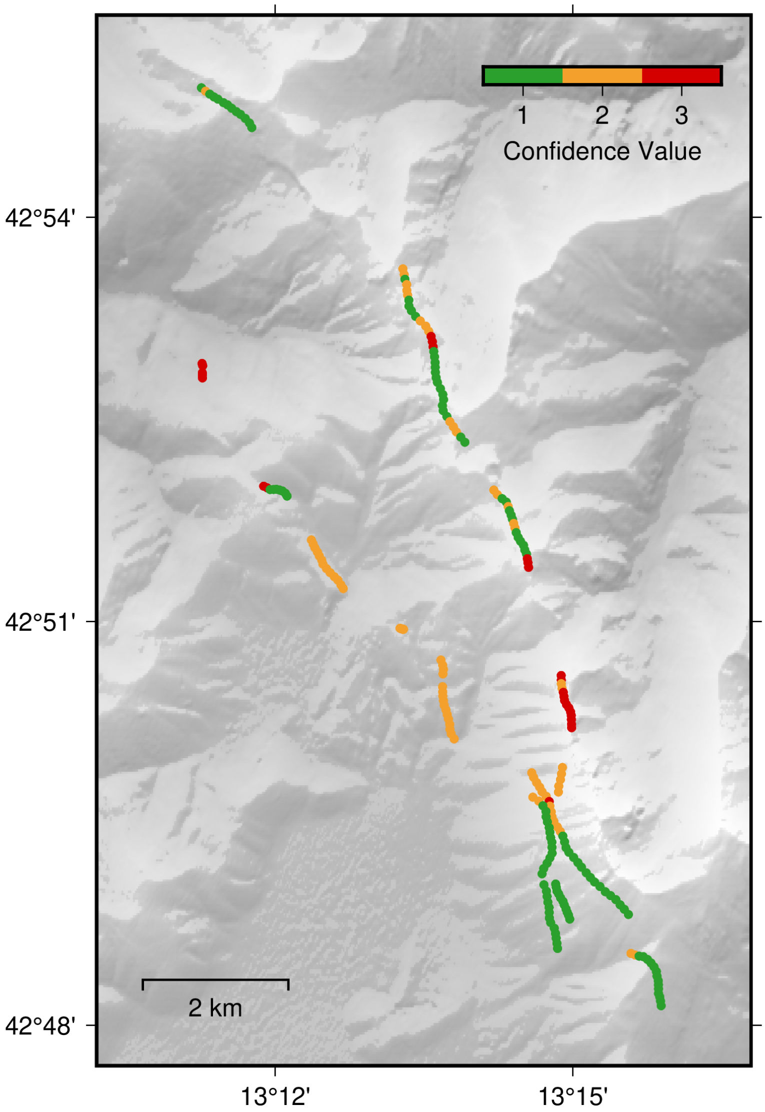

**Figure S4.** Confidence value for each optical offset measured. Value of 1, 2 and 3 indicate good, medium, and poor offset confidence, respectively. See main text and Figure S3 for explanations.

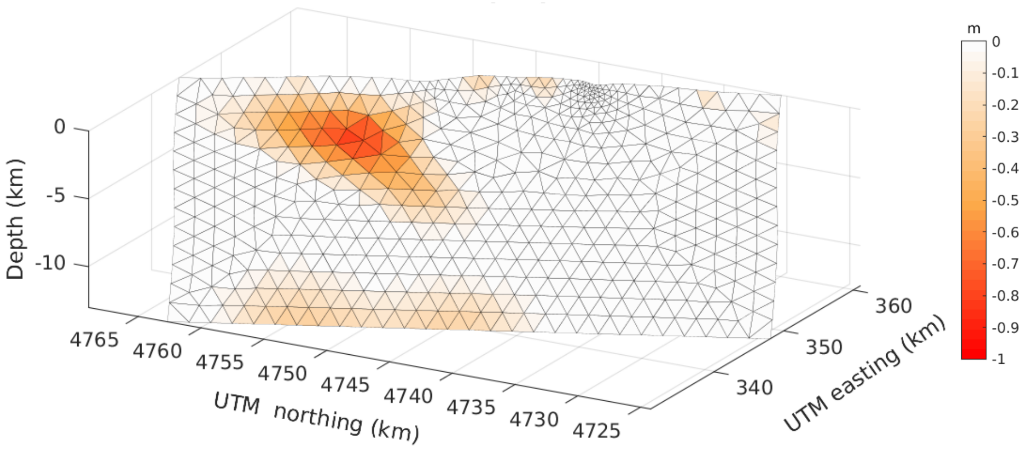

a. Visso slip distribution (Mw 6.0)

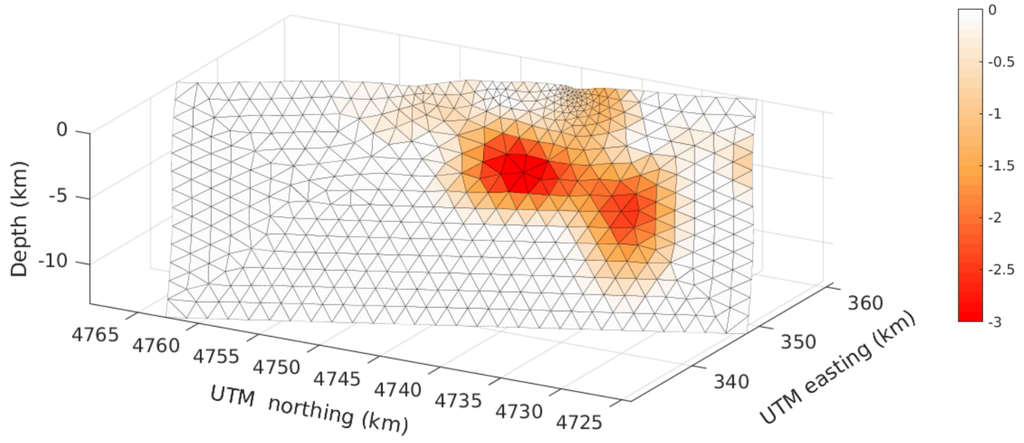

b. Norcia slip distribution (Mw 6.5)

**Figure S5.** Slip distributions of the (a) Visso and (b) Norcia earthquakes from the joint inversion of InSAR and GPS data. See supplementary text S1 for details.

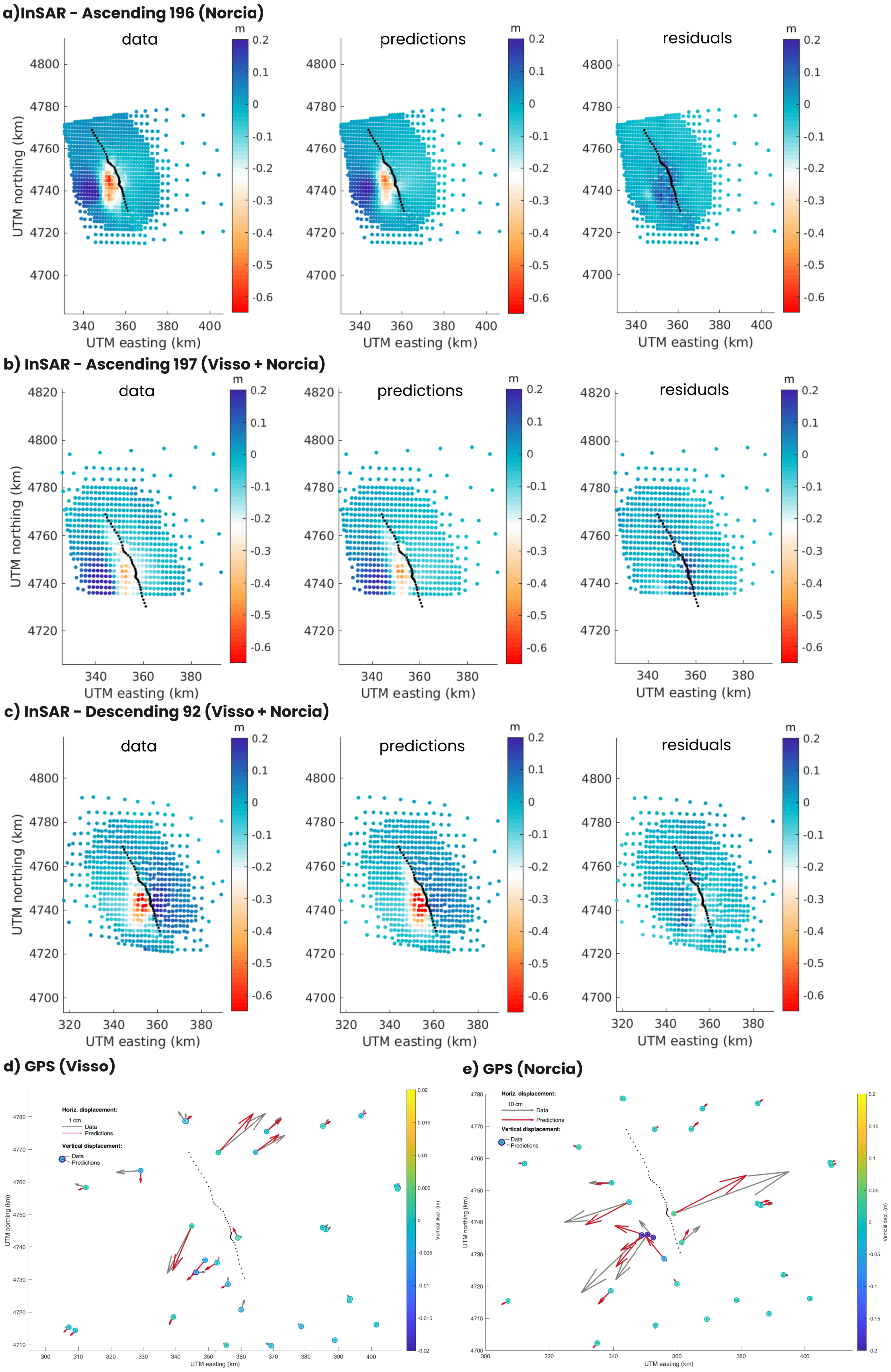

**Figure S6.** Data, model predictions, and residuals for the joint inversion for the Visso and Norcia slip distributions (see supplementary text S1).

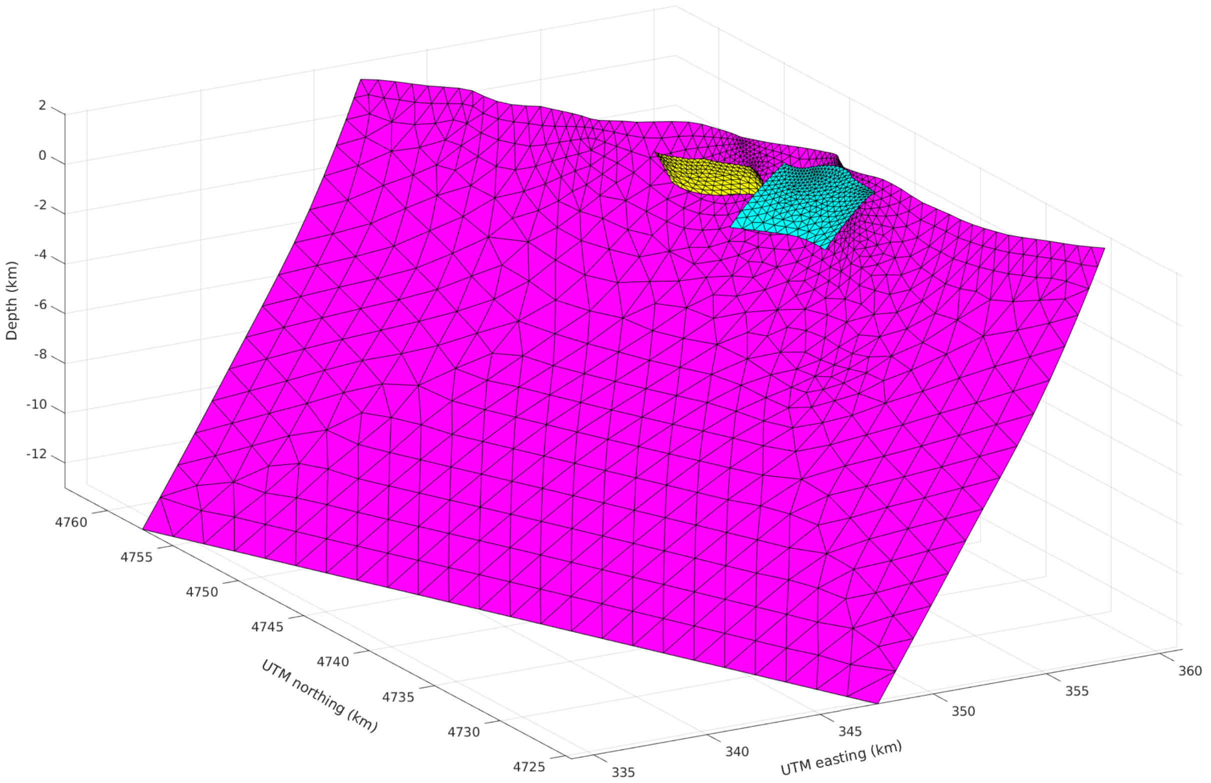

**Figure S7.** 3D representation of the fault geometry of our preferred model

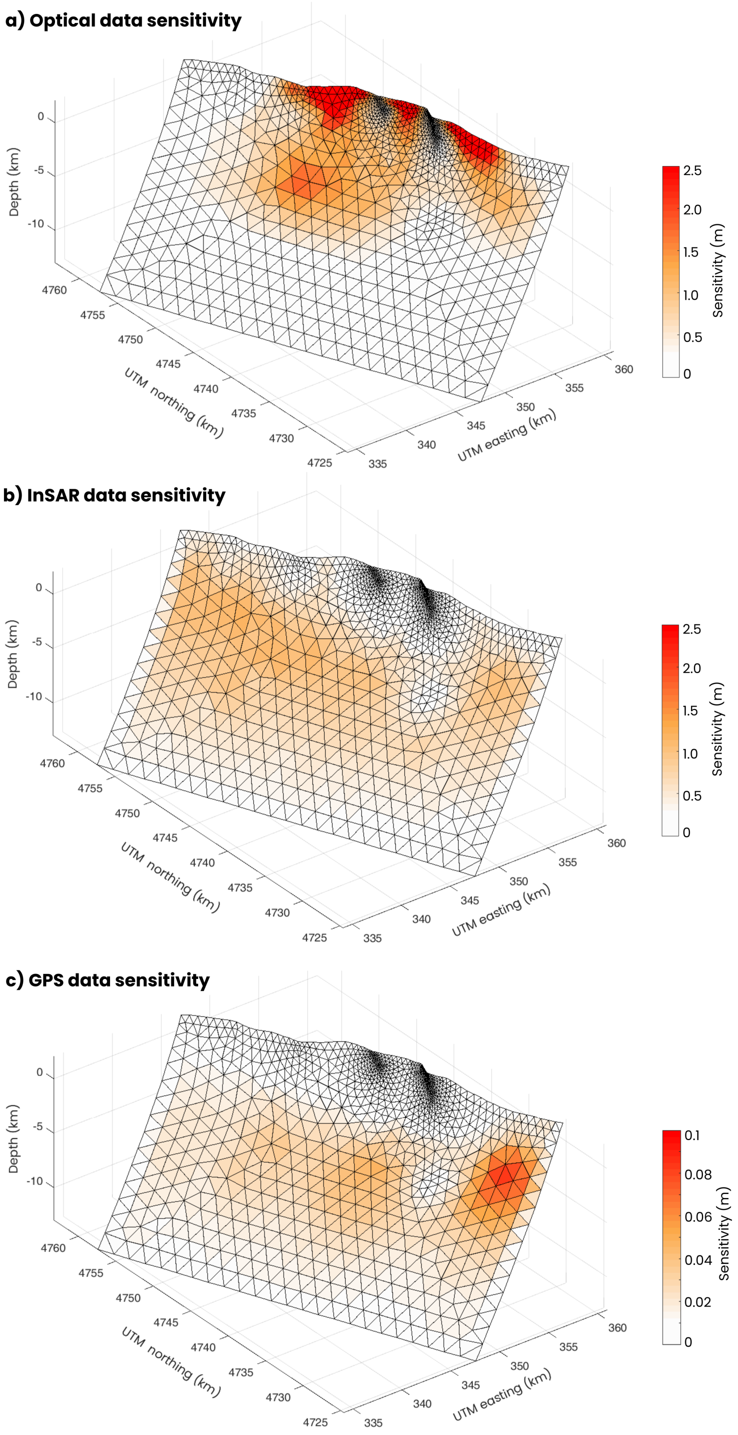

**Figure S8.** Sensitivity of the (a) optical, (b) InSAR and (c) GPS data for the main fault.

**a) Optical data sensitivity**

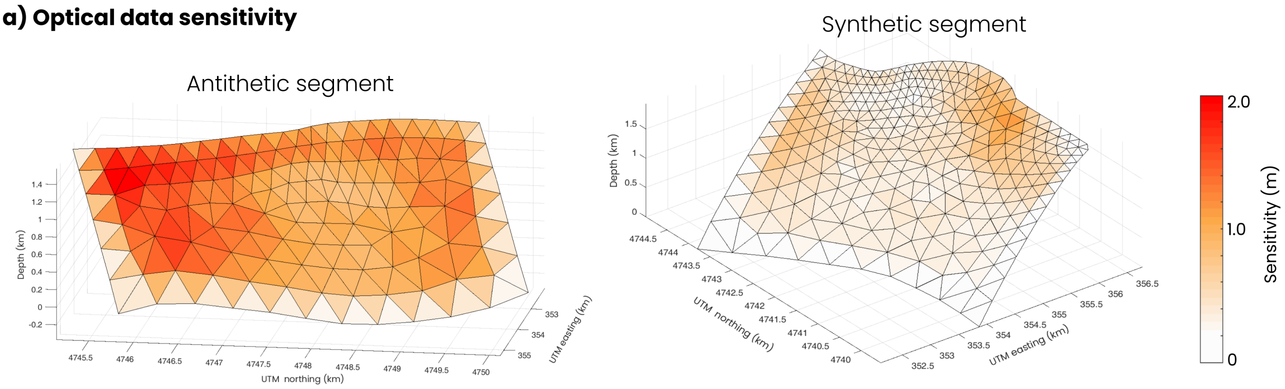

**b) InSAR data sensitivity**

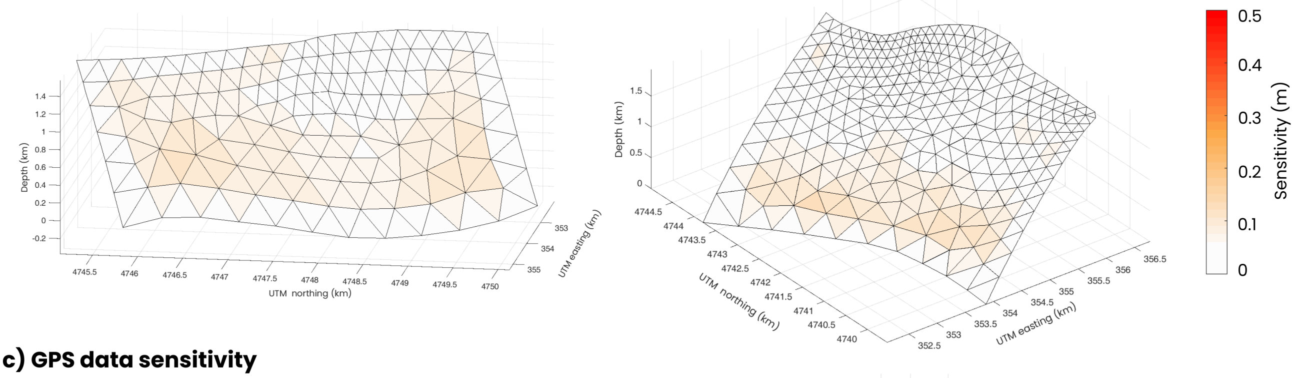

**c) GPS data sensitivity**

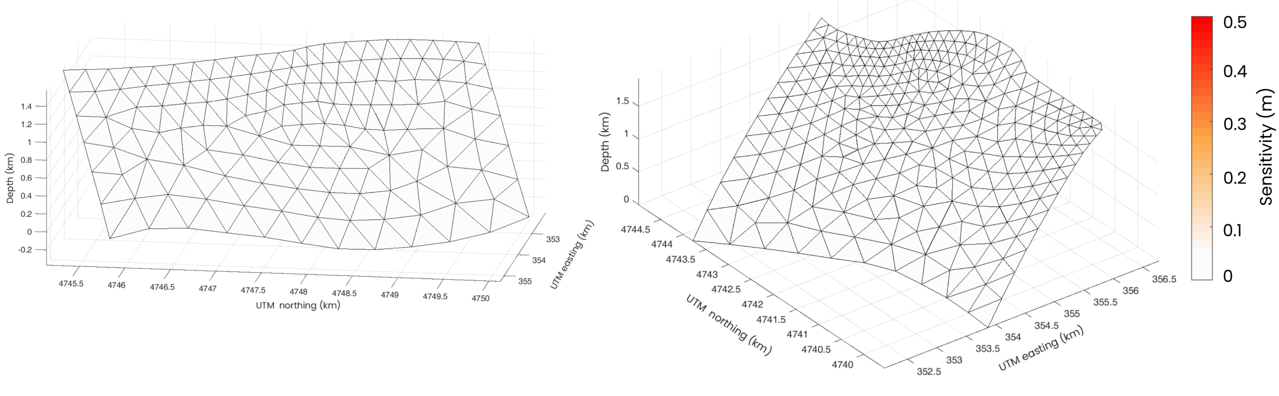

**Figure S9.** Sensitivity of the (a) optical, (b) InSAR and (c) GPS data for the secondary faults.

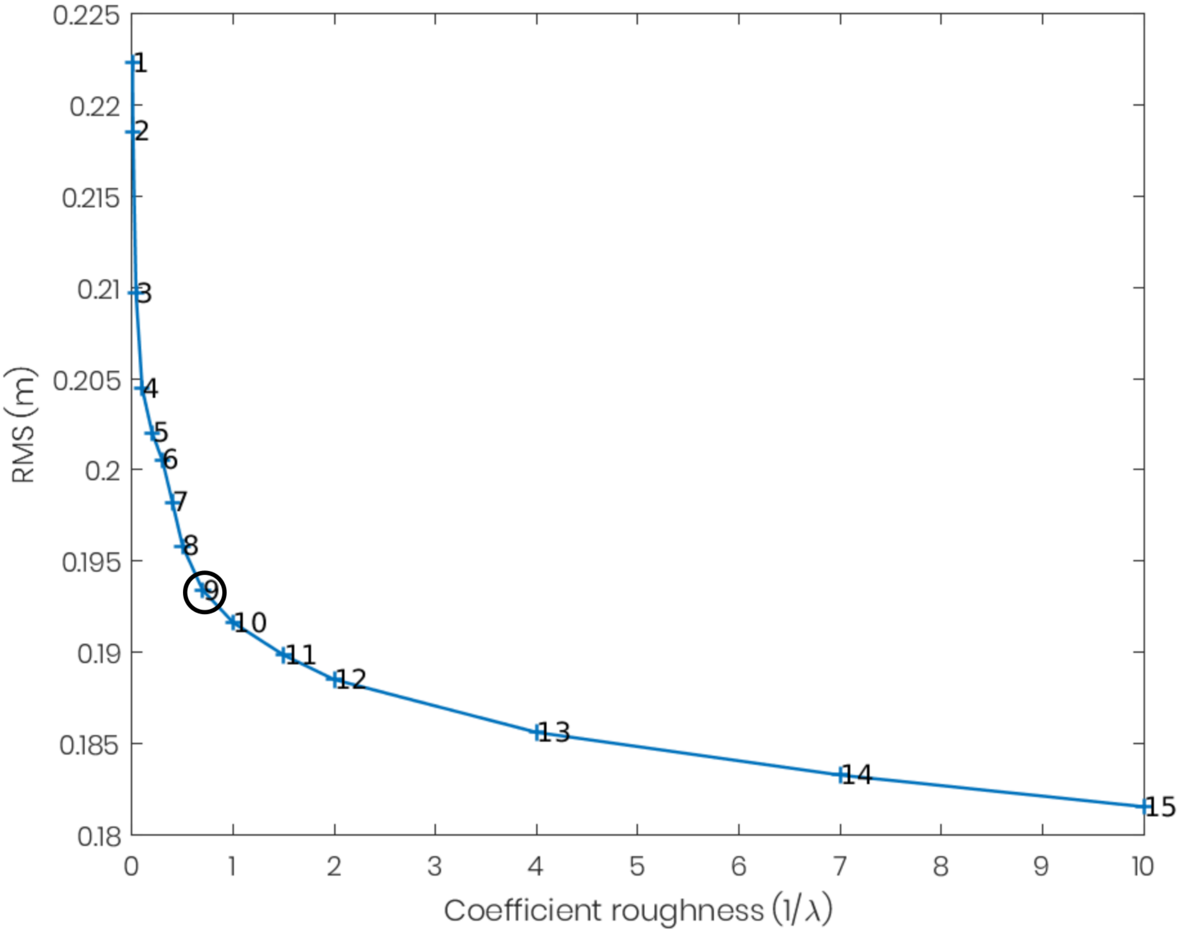

**Figure S10.** Data misfit as a function of roughness coefficient. The chosen roughness coefficient is indicated by the black circle.

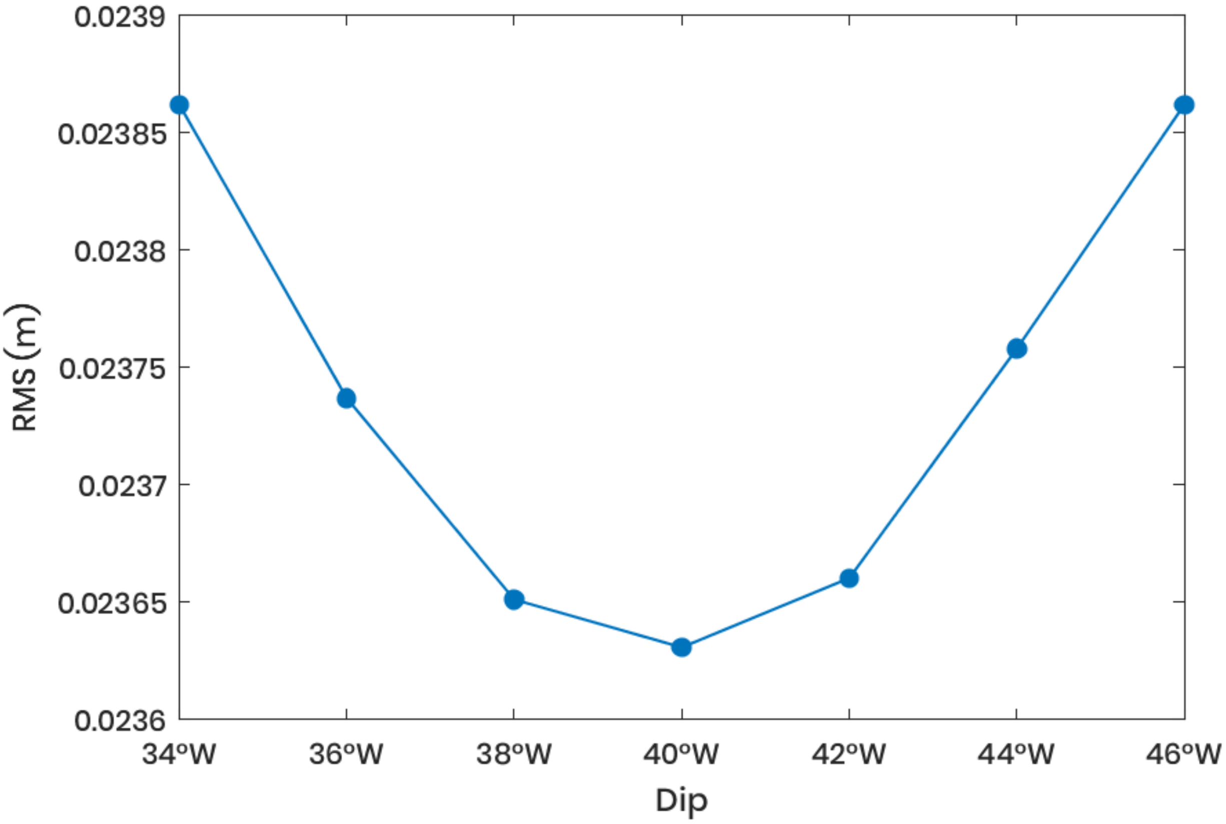

**Figure S11.** Data misfit as a function of the main fault dip angle. The lowest RMS value is reached for a dip angle of 40°W

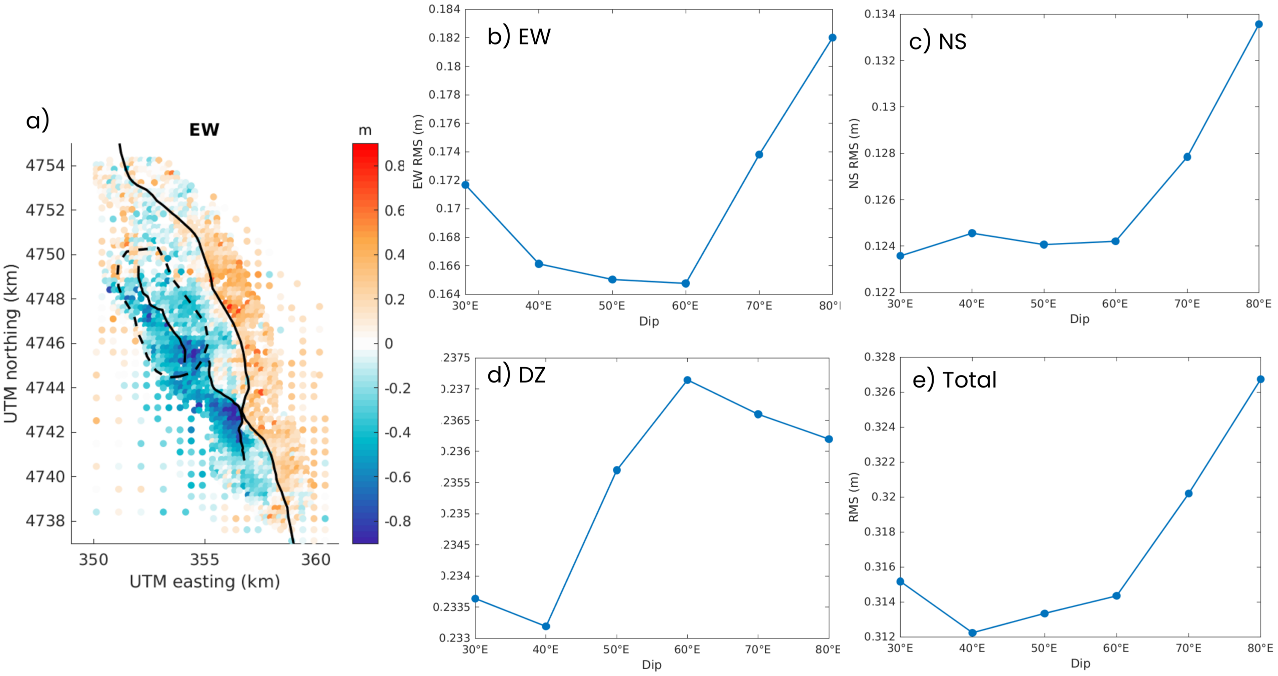

**Figure S12.** Dip angle estimation for the antithetic secondary segment. Due to the limited size of the secondary segments, varying their dip angles does not affect significantly the total RMS. For these segments, we therefore compute the RMS on a small area of the optical dataset. (a) EW optical displacement field showing the area used to compute the RMS (dotted line). (b-c) RMS as a function of the antithetic segment dip angle for the EW, NS and DZ optical data, respectively. (d) Total RMS. The best dip angle value is 40°E.

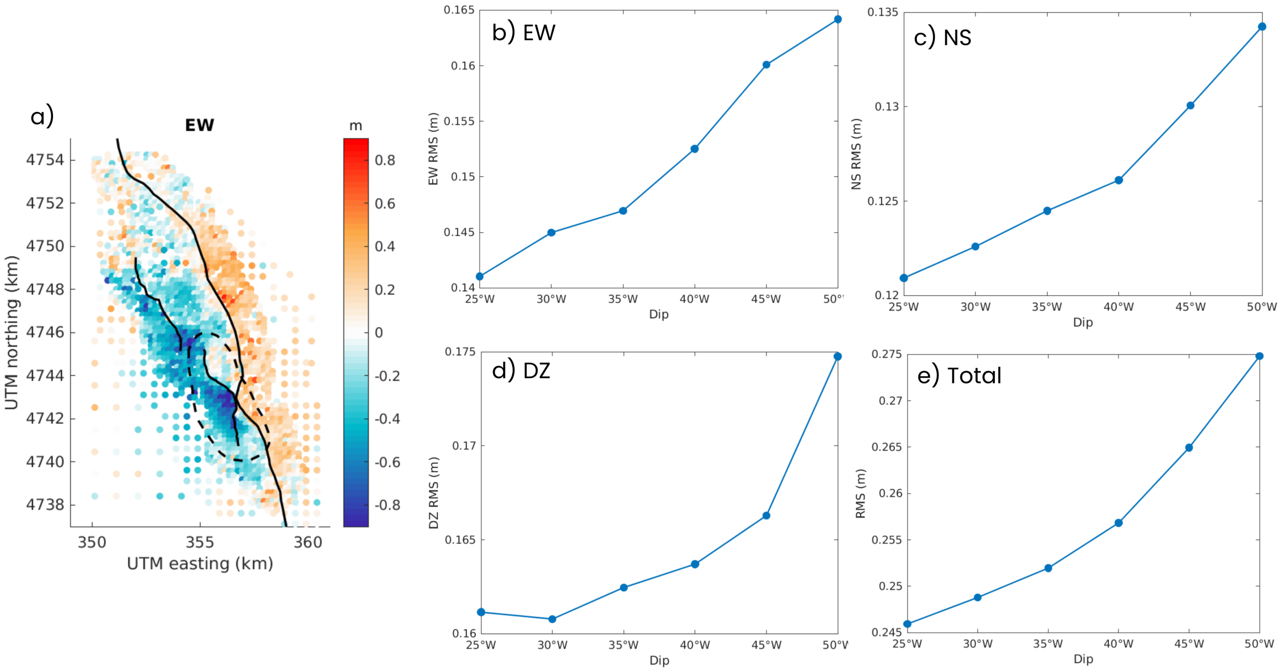

**Figure S13.** Dip angle estimation for the synthetic secondary segment. Due to the limited size of the secondary segments, varying their dip angles does not affect significantly the total RMS. For these segments, we therefore compute the RMS on a small area of the optical dataset. (a) EW optical displacement field showing the area used to compute the RMS (dotted line). (b-c) RMS as a function of the synthetic segment dip angle for the EW, NS and DZ optical data, respectively. (d) Total RMS. The EW and NS components of the optical data favor a dip angle $\leq$ to 25°W while the DZ component favors a 30°W dip angle. Considering a $\leq$ 25°W dip angle unrealistic, we here choose a dip angle of 30°W for this segment.

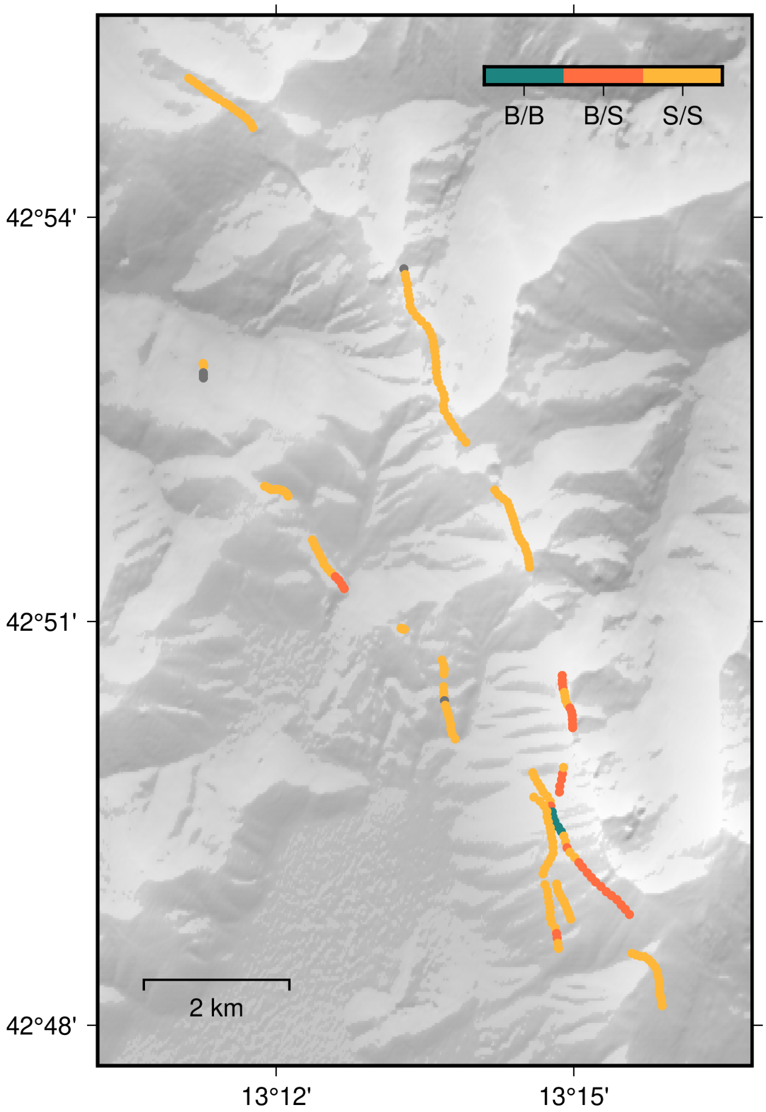

**Figure S14.** Rock type interface for each offset measured. B/B, B/S, and S/S mean that the rupture goes through bedrock on both sides of the fault, bedrock on one side and unconsolidated materials or soil on the other, and unconsolidated materials or soil on both sides of the fault, respectively. Data points for which the information is not known are plotted in gray. See main text for explanations.

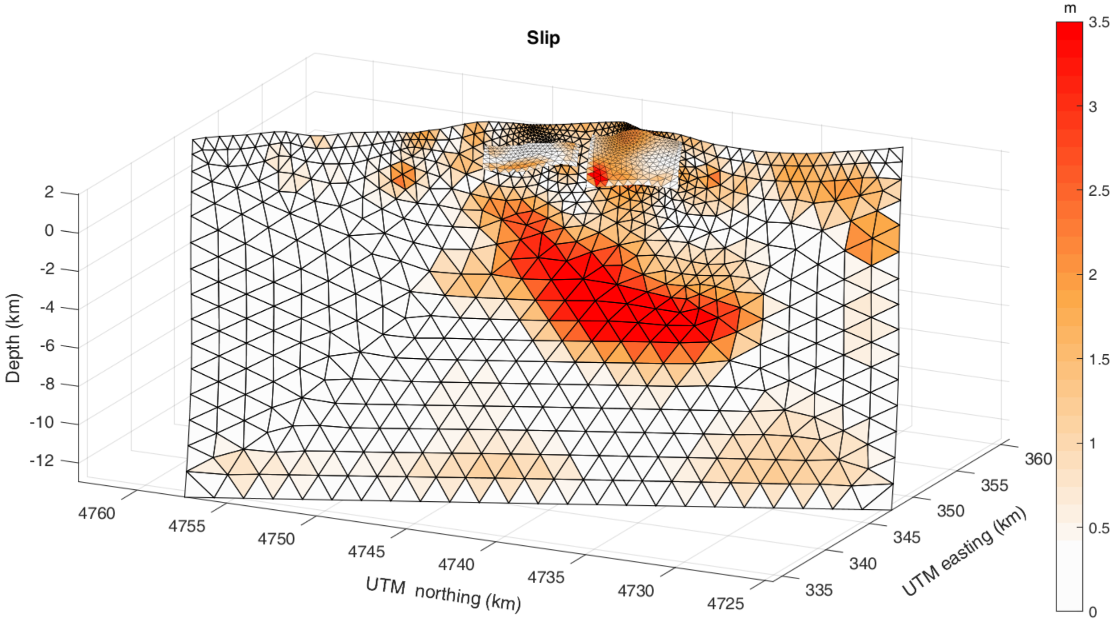

**Figure S15.** Slip model obtained from the InSAR data alone, showing that the slip pattern and amplitude change considerably compared to the joint-data model.

**Table S1.** Metadata of the optical images used to measure the 3D surface displacement field of the Norcia earthquake

| Displacement map | Sensor | Spatial resolution (m) | Date (dd.mm.yyyy) | Time span |
|---|---|---|---|---|
| Coseismic correlation | Pléiades | 0.5 | 29.10.2016 | 3 days |
| | WorldView-2 | 0.5 | 01.11.2016 | |
| Postseismic correlation (for aliasing correction) | WorldView-2 | 0.5 | 01.11.2016 | ~10.5 months |
| | Pléiades | 0.5 | 13.09.2017 | |

**Table S2.** Metadata of the ALOS-2 interferograms

| Orbit Direction | Track | Event(s) encompassed | Pre-date (dd.mm.yyyy) | Post-date (dd.mm.yyyy) |
|---|---|---|---|---|
| Descending | 92 | Norcia & Visso | 31.08.2016 | 09.11.2016 |
| Ascending | 197 | Norcia & Visso | 24.08.2016 | 02.11.2016 |
| Ascending | 196 | Norcia | 28.10.2016 | 11.11.2016 |

**Table S3.** Mean, minimum, and maximum offset values for each segment measured from the optical displacement field and in the field (Villani et al. (2018)

| | Optical offset (m) | | | Field offset (m) | | |
|---|---|---|---|---|---|---|
| Segment | Mean | Min | Max | Mean | Min | Max |
| 1 | 0.25 | 0.12 | 0.34 | 0.24 | 0.17 | 0.3 |
| 2 | 0.53 | 0.23 | 0.81 | 0.29 | 0.13 | 0.55 |
| 3 | 0.46 | 0.01 | 0.61 | 0.13 | 0.08 | 0.21 |
| 4 | 0.04 | -0.15 | 0.2 | 0.17 | 0.05 | 0.26 |
| 7 | 0.64 | 0.11 | 1.11 | 0.89 | 0.18 | 1.48 |
| 8 | 0.45 | 0.28 | 0.53 | 0.31 | 0.22 | 0.4 |
| 9 | -0.52 | -0.62 | -0.39 | 0.17 | 0.14 | 0.18 |
| 10 | 0.59 | 0.33 | 0.81 | 0.46 | 0.19 | 0.95 |
| 11 | 0.3 | 0.12 | 0.49 | 0.18 | 0.03 | 0.41 |
| 12 | -0.36 | -0.38 | -0.32 | 0.12 | 0.12 | 0.12 |
| 13 | -0.64 | -0.86 | -0.43 | 0.46 | 0.25 | 0.65 |
| 14 | -0.53 | -0.73 | -0.16 | 0.29 | 0.27 | 0.3 |
| 15 | 0.01 | -0.05 | 0.07 | 0.22 | 0.22 | 0.22 |